# CALIBRATION AND PERFORMANCE OF THE TIME-OF-FLIGHT SYSTEM USED IN THE STUDY OF THE EXCLUSIVE $\vec{n}p \rightarrow pp(\pi^-)$ REACTION

by

Ali Mahmoud Amer

A thesis
presented to the University of Manitoba
in partial fulfillment of the
requirements for the degree of
Master of Science
in
PHYSICS

Winnipeg, Manitoba, Canada 1993

National Library
of Canada

Acquisitions and
Bibliographic Services Branch

395 Wellington Street
Ottawa, Ontario
K1A 0N4

Bibliothèque nationale
du Canada

Direction des acquisitions et
des services bibliographiques

395, rue Wellington
Ottawa (Ontario)
K1A 0N4

*Your file Votre référence*

*Our file Notre référence*



ISBN 0-315-81755-0

Canada

# Student Future Work Form

Each year Graduate Studies compiles statistics about the employment of graduating students. Would you please assist us by asking the student about future plans and completing this form.

PLEASE CHECK ONE SQUARE ONLY

STUDENT'S NAME _____

DEPARTMENT _____

DEGREE _____

CITIZENSHIP STATUS* _____

COUNTRY OF ORIGIN _____

| **Employment:** | Manitoba | Rest of Canada | Home Country** | Others** | U.S.A. | Unknown |
|---|---|---|---|---|---|---|
| Industry | | | | | | |
| Self-employed | | | | | | |
| Government — Provincial | | | | | | |
| Government — Federal | | | | | | |
| University teaching, U. of Manitoba | | | | | | |
| University teaching, Elsewhere | | | | | | |
| University — other than teaching, U. of Manitoba | | | | | | |
| University — other than teaching, Elsewhere | | | | | | |
| College teaching*** | | | | | | |
| High School teaching | | | | | | |
| **Continuing Education:** | | | | | | |
| Continuing full-time student, U. of Man. | | | | | | |
| Continuing full-time student, Elsewhere | | | | | | |
| Continuing part-time student, U. of Man. | | | | | | |
| Continuing part-time student, Elsewhere | | | | | | |
| Post-Doctoral Fellow — U. of Manitoba | | | | | | |
| Post-Doctoral Fellow — Elsewhere | | | | | | |
| Post-Doctoral Fellow — Industrial | | | | | | |
| Research (other than above) | | | | | | |
| Unemployed | | | | | | |
| Other | | | | | | |

* Citizenship status: Canadian, Landed Immigrant, Student Visa
** Please indicate which country
*** College teaching includes Community Colleges

# CALIBRATION AND PERFORMANCE OF THE TIME-OF-FLIGHT SYSTEM USED IN THE STUDY OF THE EXCLUSIVE $\vec{n}p \rightarrow pp\pi^-$ REACTION

BY

ALI MAHMOUD AMER

A Thesis submitted to the Faculty of Graduate Studies of the University of Manitoba in partial fulfillment of the requirements for the degree of

MASTER OF SCIENCE

# Abstract

Calibration and performance of the Time-Of-Flight (TOF) system, that was used in the recent TRIUMF experiment studying the $\vec{n}p \rightarrow pp\pi^-$ reaction, is presented. The TOF system consisted of a start scintillator (S1) and a segmented stop scintillator (S2) made up of 18 bars of Bicron-408 each $200 \times 100 \times 3\ cm^3$.

The calibration was concerned with determining constants which enable the calculation of the absolute values of impact position, time of flight, and energy loss for charged particles passing through the TOF system. The main calibration constants that were determined are: an effective light speed of $15.5 \pm 0.5\ cm/ns$, and an effective light attenuation length of $195 \pm 10\ cm$.

The performance of the TOF system was also investigated for the entire period of experiment, an overall time resolution of $\sigma = 230\ ps$ was obtained for most of the bars.

# Acknowledgements

I would like to express my appreciation and gratitude to my advisor, professor Norm Davison, for his support, encouragement, and advise during the course of this work. I also wish to extend my thanks to Mark Bachman, Des Ramsay for the time they took to answer my questions and requests, and to all the intermediate energy group at the University of Manitoba, without whom this work would have been impossible.

Special thanks to my dear wife and children for their patience, understanding, and support, and to my beloved parents and beloved brothers for their continuous encouragement and moral support.

# TABLE OF CONTENTS

CHAPTER PAGE

# LIST OF FIGURES

FIGURE PAGE

# LIST OF TABLES

# Nomenclature

## Abbreviations

| | |
|---|---|
| PIPROD | The TRIUMF 372 experiment ($\vec{n}p \rightarrow pp\pi^-$). |
| S1 | Start scintillator of the time-of-flight system. |
| S2 | Stop scintillator of the time-of-flight system. |
| TOF | Time of flight of a charged particle between the S1 and S2 scintillators. |
| PMT | Photomultiplier tube; a device used to convert the light output of a scintillator into an electrical signal. |
| TDC | Time-to-digital converter; a device used to measure the time from a leading edge of a common start pulse to the leading edge of its individual stop pulse. |
| ADC | Analog-to-digital converter; a device used to measure the height of an analog signal. |
| CAMAC | Computer automated measurement and control; a data acquisition system. |
| TLD | Thin logic device; a delay line chamber used to signal the passage of a charged particle through it. |
| DC | Drift chamber; a device used to determine the trajectory of a charged particle that goes through it. |
| $LH_2$ | Liquid hydrogen. |
| $LD_2$ | Liquid deuterium. |
| $CH_2$ | Polyethylene $(CH_2)_n$. |
| FWHM | Full width at half maximum. |

## Symbols

| | |
|---|---|
| $N$ | Normal to the scattering plane direction of the polarization. |
| $L$ | Along the beam line direction of the polarization. |
| $S$ | In the scattering plane and perpendicular to the beam line sideway direction of the polarization. |
| $\pi$ | Pion |
| $\eta_m$ | maximum pion momentum in units of pion mass. |
| $I$ | Isospin; a quantum number which distinguishes between particles that behave in the same way with respect to strong forces, but have different charges |
| $V_{eff}$ | effective velocity of light inside a scintillator. |
| $\lambda$ | Attenuation coefficient; a parameter used to account for the absorption of scintillation light in a scintillator. |
| $dE/dX$ | Stopping power; the magnitude of energy loss per unit length. |

# CHAPTER 1

# Introduction

Since single pion production is the only significant inelastic channel in the nucleon-nucleon collision below 1 $GeV$, the study of this subject is of fundamental importance to the understanding of the nucleon-nucleon interaction and to the development of a consistent theory which is valid both below and above single pion production threshold ($\sim 290\ MeV$).

In the past two decades there has been a considerable progress in the experimental and theoretical investigation of single pion production. On the experimental side, a number of experiments measuring differential cross sections and spin dependent observables in exclusive kinematics have been performed, particularly, of the proton-proton reactions $pp \rightarrow d\pi^+$ and $pp \rightarrow np\pi^+$. On the theoretical side, more advanced models describing several coupled reaction channels within a unified theory have been developed. These models have been able to describe the gross features of the data, but they fail to give a quantitative description of some observables [Set92].

## 1.1 Isospin reaction Cross Section

Using isospin conservation, Rosenfeld [Ros54] showed that the total cross sections for pion production reactions from nucleon-nucleon collisions could be decomposed into three partial cross sections. These cross sections are denoted by $\sigma_{if}$ where $i$ is the initial and $f$ is the final isotopic spin of the two-nucleon system.

Table 1.1: Isotopic spin decomposition for total cross sections.

| Reaction | Isotopic spin decomposition |
|---|---|
| $p+p \rightarrow d+\pi^+$ | $\sigma_{10}(d)$ |
| $p+p \rightarrow n+p+\pi^+$ | $\sigma_{10}(np)+\sigma_{11}$ |
| $p+p \rightarrow p+p+\pi^0$ | $\sigma_{11}$ |
| $n+p \rightarrow d+\pi^0$ | $\frac{1}{2}\sigma_{10}(d)$ |
| $n+p \rightarrow n+p+\pi^0$ | $\frac{1}{2}[\sigma_{10}(np)+\sigma_{01}]$ |
| $n+p \rightarrow n+n+\pi^+$ | $\frac{1}{2}[\sigma_{11}+\sigma_{01}]$ |
| $n+p \rightarrow p+p+\pi^-$ | $\frac{1}{2}[\sigma_{11}+\sigma_{01}]$ |

To indicate the production of a bound and unbound neutron and proton in the final state, $\sigma_{10}$ is written as $\sigma_{10}(d)$ and $\sigma_{10}(np)$ respectively.

The decomposition of the total cross sections for the different pion production reactions, as adapted from [Ros54], is given in table 1.1. These relations are subject to small corrections due to coulomb interactions which break isospin symmetry. However, these corrections are smaller than the uncertainty of the data in most cases.

A few points can be noted from table 1.1 :

1. There is no $\sigma_{00}$, because the pion with isotopic spin of 1 cannot combine with a final state nucleon pair with isospin 0 to give a total final state isospin of 0.

2. The cross sections for the production of $nn\pi^+$ and $pp\pi^-$ final states should be equal (assuming that isospin conservation holds).

3. For the $np \rightarrow pp\pi^-$ reaction, both isospin channels, I=0 and I=1, are open.

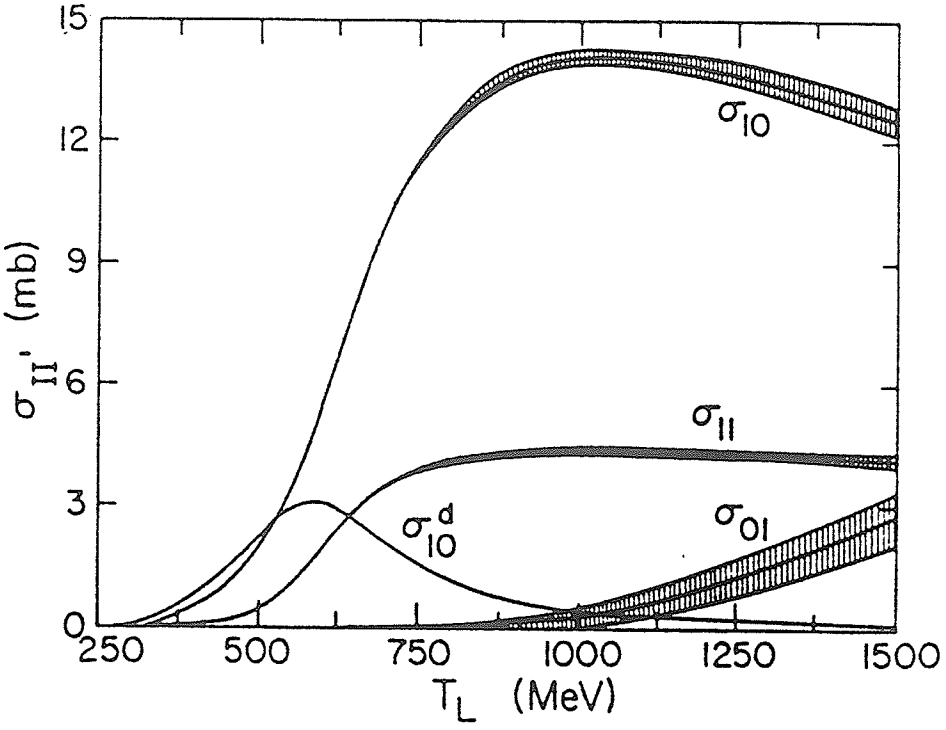


Figure 1.1: Energy dependence of the partial isospin reaction cross sections (from [Ver82]).

4. All the partial cross sections can be determined from proton-proton collisions, except $\sigma_{01}$ which can be studied only in neutron-proton collisions.

Using the available experimental data from single pion production reactions, Ver West and Arndt preformed a phase shift analysis and determined the isospin cross sections [Ver82]. The energy dependences of these cross sections are shown in figure 1.1. It should be pointed out that there still exists some inconsistency concerning the value of $\sigma_{01}$ (see section 1.3.2 for more discussion).

### 1.1.1 Intensity Classes

Rosenfeld [Ros54] also showed that the independent partial cross sections $\sigma_{10}(d)$, $\sigma_{10}(np)$, $\sigma_{11}$, and $\sigma_{01}$ could be divided into several "intensity classes" according to the angular momentum of the two-nucleon system and that of the pion. Near the threshold region only $l < 2$ needs to be considered and hence the intensity classes are denoted by Sp, Ss, Pp, and Ps (in order of decreasing intensity). The first letter refers to the relative angular momentum of the two nucleons in the final state and the second letter refers to the angular momentum of the pion with respect to the center of mass of the two nucleons. A list of the intensity classes that contribute to the $np \rightarrow pp\pi^-$ isospin cross sections, $\sigma_{01}$ and $\sigma_{11}$, is given in table 1.2.

In this table the initial and the final states of the two nucleons are described using the usual notation of $^{2S+1}L_J$ where S is the spin, L is the orbital angular momentum and J is the total angular momentum of the two nucleons. The state of the pion is described by $l_j$ where $l$ donates the orbital angular momentum of the pion and $j$ expresses the total angular momentum of the final state.

Provided that there is no interference between the various states, the angular distribution of the pions would be

- Isotropic; if the total angular momentum is zero or if the pion is produced in an $s$ state.
- $C+\cos^2(\theta)$; if the total angular momentum $j \geq 1$, and if the pion is produced in a $p$ state.

The expected angular distribution for each transition is shown in column five of table 1.2.

For energies up to 400 or 500 $MeV$, Gell-Mann and Watson [Gel54] calculated

Table 1.2: Transitions of low partial waves which represent the $np \rightarrow pp\pi^-$ reaction.

| Isotopic reaction | Class | Initial state | Final state | Angular distribution | Energy dependence |
|---|---|---|---|---|---|
| $\sigma_{11}$ | Sp | none | ${}^1S_0p_1$ | ... | 0 |
| | Ss | ${}^3P_0$ | ${}^1S_0s_0$ | Isotropic | $\eta_m^2$ |
| | Pp | ${}^3P_1$ | ${}^3P_0p_1$ | $C+\cos^2(\theta)$ | $\eta_m^8$ |
| | | ${}^3P_{0,1,2}$ or ${}^3F_2$ | ${}^3P_1p_{0,1,2}$ | $C+\cos^2(\theta)$ | $\eta_m^8$ |
| | | ${}^3P_{1,2}$ or ${}^3F_{2,3}$ | ${}^3P_2p_{1,2,3}$ | $C+\cos^2(\theta)$ | $\eta_m^8$ |
| | Ps | ${}^1S_0$ | ${}^3P_0s_0$ | Isotropic | $\eta_m^6$ |
| | | ${}^1D_2$ | ${}^3P_2s_2$ | Isotropic | $\eta_m^6$ |
| $\sigma_{01}$ | Sp | ${}^3S_1$ or ${}^3D_1$ | ${}^1S_0p_1$ | $C+\cos^2(\theta)$ | $\eta_m^4$ |
| | Ss | none | ${}^1S_0s_0$ | ... | 0 |
| | Pp | ${}^1P_1$ | ${}^3P_{0,1,2}p_1$ | $C+\cos^2(\theta)$ | $\eta_m^8$ |
| | | ${}^1F_3$ | ${}^3P_2p_3$ | $C+\cos^2(\theta)$ | $\eta_m^8$ |
| | Ps | ${}^3S_1$ or ${}^3D_1$ | ${}^3P_1s_1$ | Isotropic | $\eta_m^6$ |
| | | ${}^3D_1$ | ${}^3P_2s_2$ | Isotropic | $\eta_m^6$ |

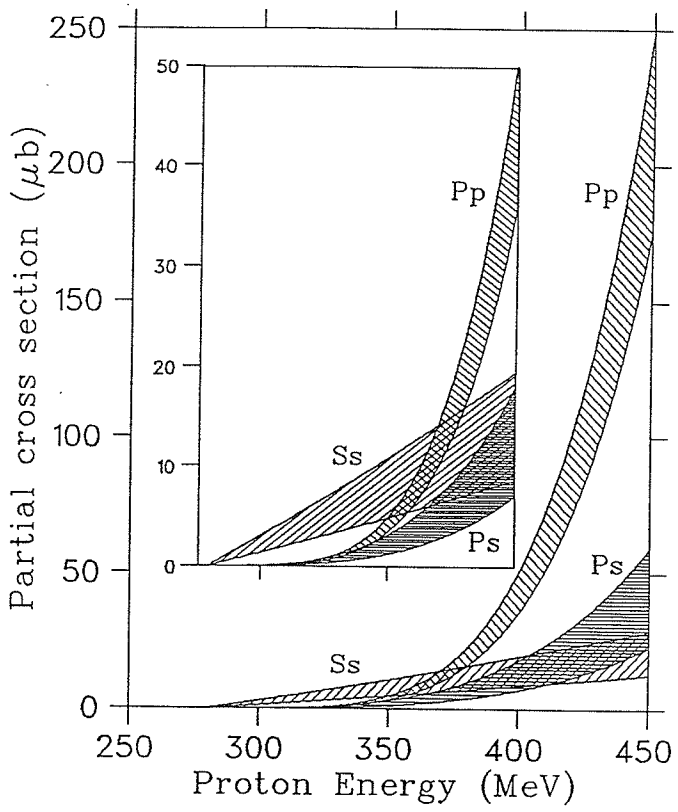


Figure 1.2: Decomposition of $\sigma_{11}$ into the low partial waves (from [Sta91])

the energy dependence for the intensity classes in terms of of the maximum pion momentum $\eta_m$ allowed in the center of mass system ($\eta_m$ is given in units of the pion mass i.e. $\eta_m = \frac{P_\pi}{(m_\pi c)}$ ). These dependences are listed in the sixth column. Stanislaus *et al.* [Sta91] analysed the energy and the angular distribution of the pions produced in the $pp \rightarrow pp\pi^0$ reaction which, in the absence of $\sigma_{01}$, is very similar to $np \rightarrow pp\pi^-$ ($\sigma_{01}$ is believed to be small or even zero at intermediate energies). They determined the strength of the low partial waves from the total cross sections as

$$\sigma_{11} = B_{Ss}\eta_m^2 + B_{Ps}\eta_m^6 + B_{Pp}\eta_m^8$$

Figure 1.2 shows their results for the contributions of the various intensity classes to $\sigma_{11}$.

## 1.2 Theoretical Situation

In this section, a brief outline of the physical content of some of the calculations used to investigate single pion production from $NN$ scattering is presented. A more detailed survey of this subject can be found in a recent review by Garcilazo and Mizutani [Gar90].

The isobar model, proposed by Mandelstam [Man58], is one of the earliest models which had some success in describing the gross features of the data. In this model, pion production is ascribed to the excitation of one of the nucleons to a delta which then breaks up into a nucleon and a pion. Most subsequent models have retained this process in their calculations.

In the one pion exchange (OPE) model, pion production is assumed to take place in two stages; first, the production of virtual pion, and then the scattering of that pion into a real one [Gar90]. The early calculations of this model [Fer63] were restricted to the I=1 channel; however, the more recent calculation by König and Kroll [Kon81], which used as input all the $\pi$N amplitudes, has investigated both I=0 and I=1 channels. The cross section predictions of [Kon81] lie systematically below the data. To account for this discrepancy, they introduced dibaryon resonances to their calculation and obtained considerable improvements. These improvements can not be taken as a proof for the existence of the dibaryon resonances, since other effects such as the opening of the $N\Delta$ channel can cause resonance-like behavior in the same energy region [Dub87].

Most of the recent theories developed in the 70's and 80's started to treat the various channels in the $NN\pi$ system

$$NN \leftrightarrow \begin{matrix} NN \\ NN\pi \\ \pi d \end{matrix} \leftrightarrow \pi d$$

in a more unified approach instead of focusing on individual $NN \rightarrow NN\pi$ reactions. Among those theories are the coupled channel ($NN - N\Delta$) method (CCM) which was pursued by Niskanen [Nis78], Matsuyama and Lee [Mat86], Garcilazo and Mathelitsch [Gar86], and Mizutani et al. [Miz87], and the coupled ($\pi NN - NN$) approach (PNNA) which was pursued mainly by Blankleider and Afnan [Bla85] and Dubach et al. [Dub87]. Even though the two theories used distinct approaches in their calculations, their final results are very similar, as can be seen in figure 1.3.

The CCM was developed by extending the conventional meson exchange theory of the nucleon-nucleon forces to include $\Delta$ excitation. The NN potential of this model is described by pion exchange plus heavy meson ($\sigma$, $\rho$, $\omega$, ...) exchanges, while the coupling between the $NN - N\Delta$ channels is described by ($\pi$ and $\rho$) exchanges only. When the mass and the decay width of the delta were incorporated in the propagators, the resulting equations were able to couple both the $NN$ and $NN\pi$ channels [Gar90]. The CCM is relativistic and preserves two-body unitarity.

The PNNA calculation, the unitary model [Klo80], was the only calculation which studied extensively both I=0 and I=1 channels, and which predicted spin observables for the exclusive $np \rightarrow pp(\pi^-)$ reaction. Its formalism and predictions will be discussed in some detail in the following subsection.

There also have been some attempts to incorporate quark effects into the calculation of the $NN \rightarrow NN\pi$ reactions [Har84,Cao86]. So far all models are in only qualitative agreement with the experimental data, and occasionally fail to reproduce even the overall structure [Set92].

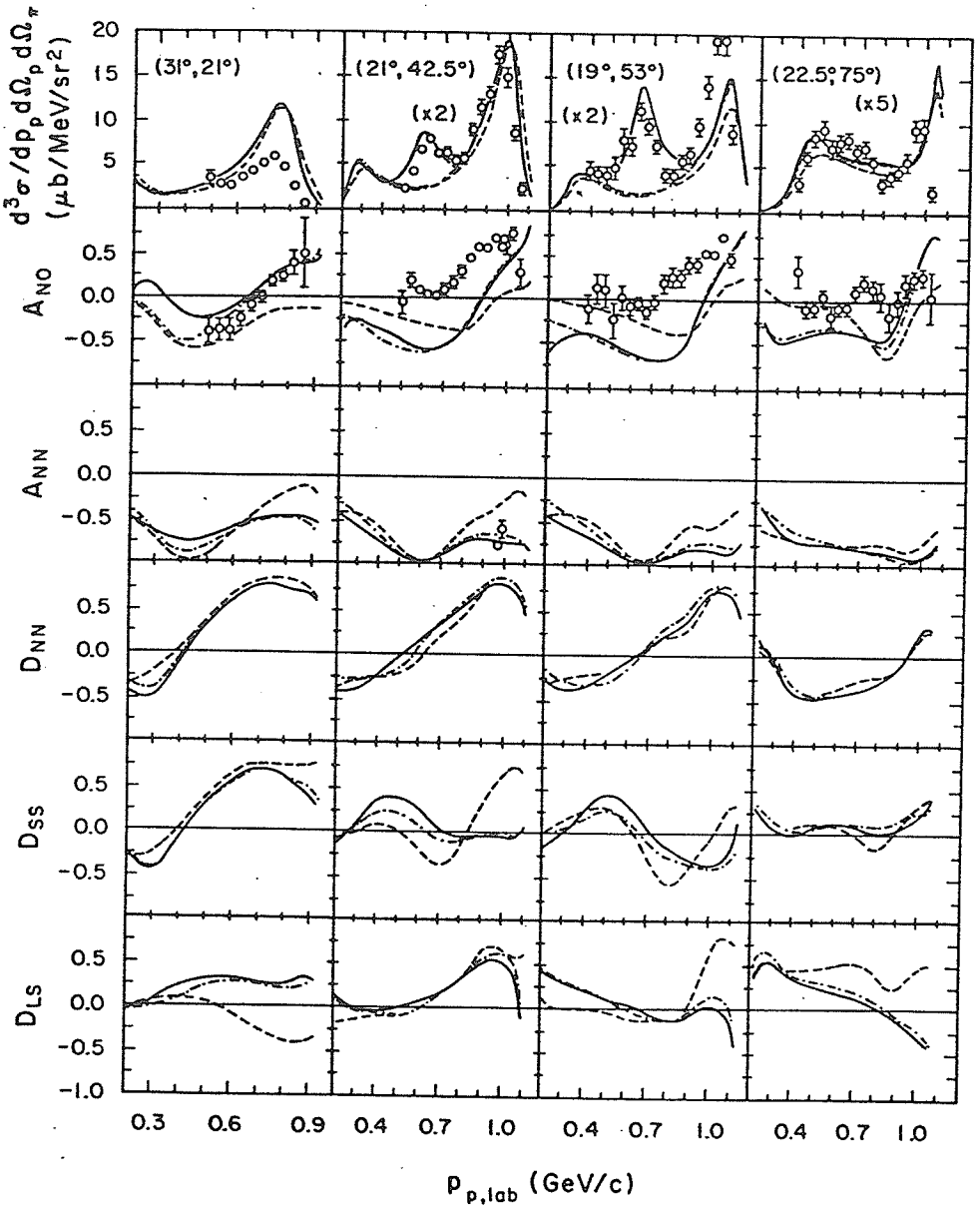


Figure 1.3: Comparison of the cross sections and spin observables as calculated in the CCM and PNNA for the exclusive reaction $pp \rightarrow p(n)\pi^+$ at 800 $MeV$ for various $(\theta_p, \theta_\pi)$ angles. Results are shown for the full unitary model of [Dub87] (solid curve), the full CCM model of [Van84] (dashed curve), and the unitary model without pion emission from $N'$ isobar (dotted-dashed curve). from [Dub86].

### 1.2.1 The Unitary Model

The unitary model, which treats elastic nucleon-nucleon scattering and single pion production in a unified way, was proposed by Kloet and Silbar [Klo80]. Their model is a modification of the three body model developed be Aaron, Amado and Young (AAY) [Aar68] to study the $\pi N \rightarrow \pi N$ and $\pi N \rightarrow \pi\pi N$ reactions.

For the $NN \rightarrow NN$ and $NN \rightarrow \pi NN$ reactions, the unitary model allows for the interaction of the pion-nucleon system in the $P_{11}(N')$ and $P_{33}(\Delta)$ channels.

$$NN \rightarrow \left\{ \begin{array}{c} NN' \\ N\Delta \end{array} \right\} \rightarrow \left\{ \begin{array}{c} NN \\ NN\pi \end{array} \right\}$$

These amplitudes are shown diagrammatically in figure 1.4. The $P_{33}$ interaction, which is dominated by the $\Delta$ resonance, was fitted to the $\pi N$ phase shift data, while the $P_{11}$ interaction was fitted to the nucleon pole and the $P_{11}$ scattering length.

The model Considers the interacting $\pi N$ systems as quasi-particles or isobars described in terms of the $T(NN \rightarrow NN')$ and $T(NN \rightarrow N\Delta)$ amplitudes. These amplitudes were calculated using a one pion exchange force. The resulting coupled equations for this system are relativistic and preserve two and three body unitarity.

Cross sections and spin observables for some exclusive and inclusive NN pion production reactions were calculated. Figure 1.3 shows a comparison of the model predictions with the experimental data for the exclusive $pp \rightarrow np\pi^+$ reactions. The overall agreement with the data is good except for the analysing power, $A_{N0}$, where the predicted values are lower than the data, but the shapes are generally correct.

Predictions for the exclusive $np \rightarrow pp\pi^-$ reaction are shown in figure 1.5. As pointed out by the authors, this reaction may well be the most important reaction

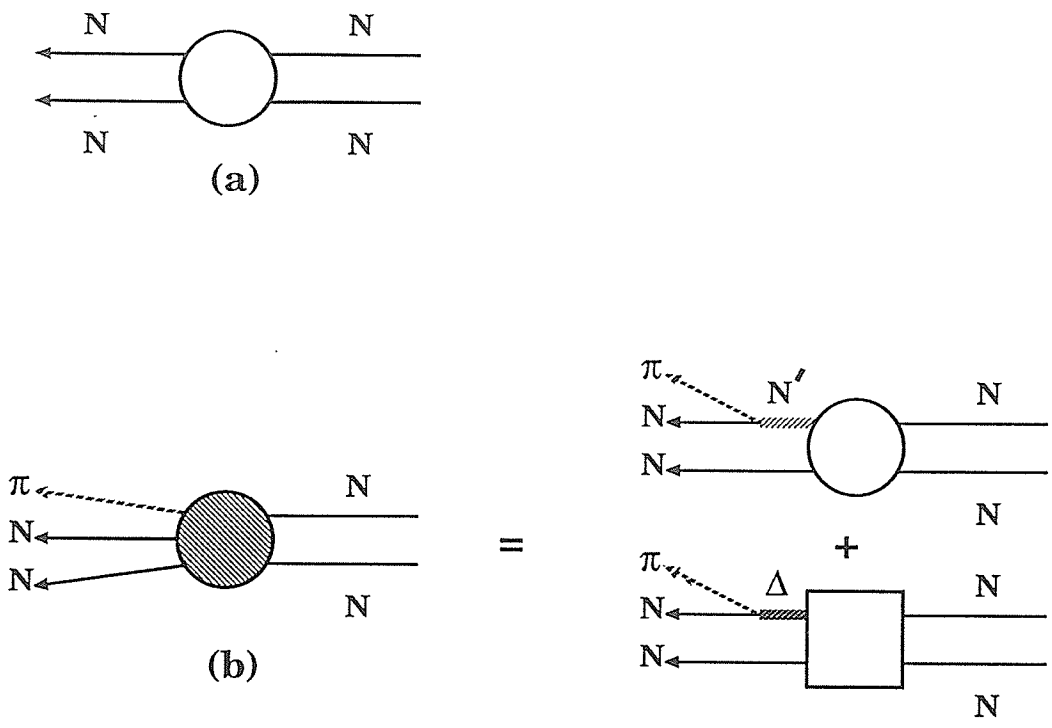


Figure 1.4: Diagrammatic representation of the isobar amplitudes used in the unitary model. (a) elastic scattering and (b) single pion production.

to study for understanding of the details of the $NN \rightarrow NN\pi$ process for the following reasons :

- Both initial isospin channels I=0 and I=1 are open, and as can be seen from figure 1.5, there is a dramatic difference between the contribution of I=0 and I=1 in most of the spin observables.

- The $\Delta^{++}$ which dominates most single pion production reactions, can not occur in the np channel due to charge non-conservation, and in the case of pion production through the I=0 initial state, the $\Delta$ resonances are not allowed at all because a delta with an isospin of 3/2 can not add with a nucleon isospin of 1/2 to give a total isospin of zero. This situation gives the opportunity for non-$\Delta$ resonances to play a more important role in pion

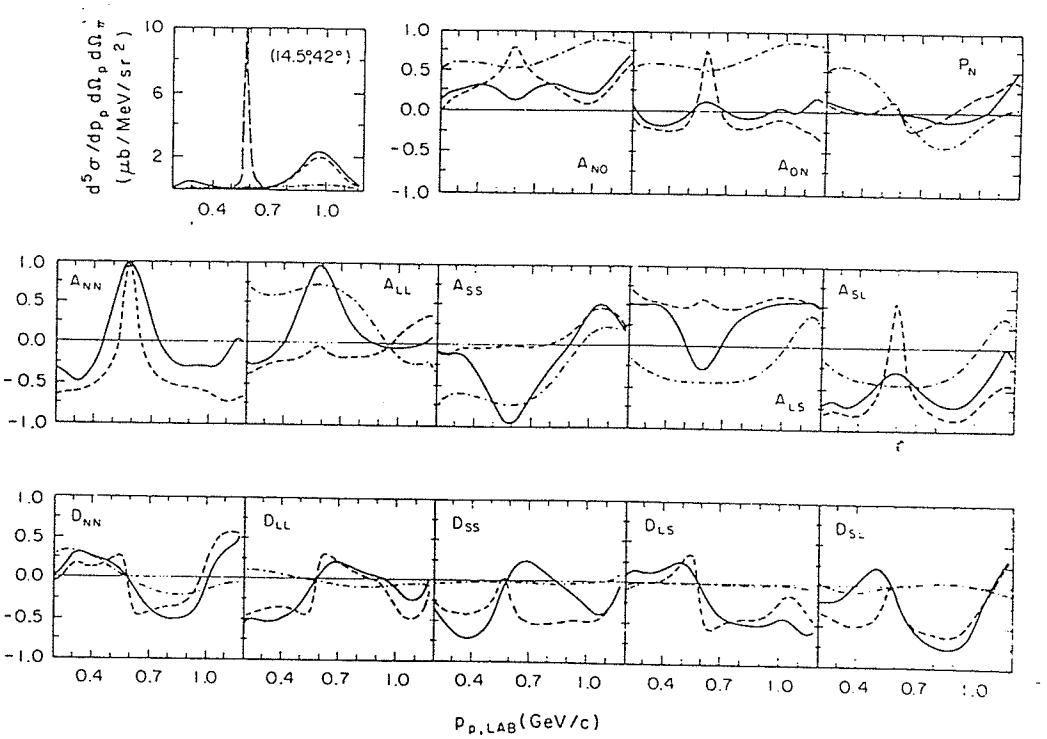


Figure 1.5: Predictions of the cross section and spin observables for the exclusive $np \rightarrow pp\pi^-$ reaction as calculated by [Dub87]. full calculation (solid curve), contribution from only I=1 states (dashed curve), and contribution from only I=0 states (dot-dashed curve).

production. Also, the interference between the $\Delta$ and non-$\Delta$ resonances results in a richer structure in spin dependent observables thereby providing an excellent ground for testing models.

## 1.3 Experimental Situation

Investigation of the $NN \rightarrow NN\pi$ reactions started in the early 1950's, but due to the low intensity beams and the nature of the detector systems used (emulsions and cloud and bubble chambers) the study of these reactions had almost stopped by the late sixties. The situation improved considerably in the 1970's and 1980's with the development of several meson factories with high intensity polarized beams and targets and with significant improvements in the detection methods allowing for the performance of kinematically complete experiments.

Another reason behind the revival of this subject was the search for dibaryon resonances in the $NN \rightarrow NN\pi$ channels. The dibaryon controversy was generated by the observation of rapid energy variations in the spin-dependent cross sections ($\Delta\sigma_T$ and $\Delta\sigma_L$) in p-p elastic scattering [Yok80]. These variations were thought to be signals of dibaryon resonances which, because of their high inelasticity, should show up clearly, if they really existed, in the inelastic channels of NN scattering. There is still no consensus on the existence of dibaryon resonances, but the most widely held opinion is that these variations can be explained by threshold effects due to the opening of the $N\Delta$ channel [Shy88].

References on most single pion production experiments performed before 1982 can be found in [Ver82]. New measurements, especially those related to the $np \rightarrow pp\pi^-$, are discussed in the following sub-sections.

### 1.3.1 p-p collision

Most of the experimental efforts in studying single pion production from $NN$ scattering were focused on the proton induced reactions, $pp \rightarrow d\pi^+$ and $pp \rightarrow np\pi^+$. A broad data base now exists for both reactions, and several amplitude

analyses have been performed which have resulted in a set of stable and well determined amplitudes.

Pion production reactions are dominated by the formation of the $\Delta(1236)$ resonance in the intermediate state which then decays into a nucleon and a pion. The isospin Clebsch-Gordan coefficients for $pp \rightarrow n\Delta^{++}$ are several times larger than those for $pp \rightarrow p\Delta^{+}$. Since the above reactions allow for the excitation of both $\Delta^{+}$ and $\Delta^{++}$, the domination of the delta is made even stronger. This feature makes both reactions a good place for testing theories, and if a theory is to have any success, it must first agree with these experimental data.

As for the $pp \rightarrow pp\pi^0$, the excitation of the $\Delta^{++}$ is not allowed (like the $np \rightarrow pp\pi^-$ reaction), hence providing the opportunity for non-delta resonances to compete with $\Delta^{+}$ and to play a more important role. The data base for this reaction has been rapidly expanding; several experiments have been recently reported in both the inclusive and exclusive $pp\pi^0$ channels.

In the inclusive channel, two experiments measuring the cross section and asymmetries for the emitted $\pi^0$ by detecting the two decay $\gamma$-rays were carried out at TRIUMF ($T_P$=320 to 500 $MeV$) [Sta91] and at Saturne ($T_P$=325 to 1012 $MeV$). Another two experiments which measured only the total cross section were also carried out: one at Saturne ($T_P$=480 to 560 $MeV$ in steps of 20 $MeV$) [Did91] and the other at LNPI (Leningrad Nuclear Physics Institute) ($T_P$=600 to 900 $MeV$ in steps of 40 to 50 $MeV$) [And88].

In the exclusive channel, Riley *et al.* carried out a kinematically complete experiment at LAMPF which measured the Wolfenstein polarization observables, the induced polarization $P_N$, and the analyzing power $A_N$ at three incident proton energies; 647, 733 and 800 $MeV$ [Ril87]. These new experiments should improve the situation for this reaction considerably, and would be very helpful in the de-

duction of the partial cross section $\sigma_{01}$.

### 1.3.2 n-p collision

The neutron-proton induced reactions are much less studied than the proton-proton ones, because of the difficulties in obtaining monoenergetic neutron beams of sufficient intensity. The early experiments performed in the n-p channel were aimed at testing the isospin invariance and charge independence in the $\pi^{\pm}$ production. Comparison of the measured cross sections of the charged and neutral pions showed that these relations are valid within experimental uncertainties.

Another subject that has been investigated is pion production from the I=0 initial state. The easiest way to determine the I=0 contribution is to compare the total cross section of the $pp \rightarrow pp\pi^0$ reaction to that of the $np \rightarrow NN\pi^{\pm}$ reactions via

$$\sigma_{01} = 2\sigma(np \rightarrow NN\pi^{\pm}) - \sigma(pp \rightarrow pp\pi^0)$$

A more sensitive indicator of the I=0 contribution is the observation of asymmetries in the $\pi^{\pm}$ differential cross sections. The differential cross section for pion production reactions can be written as

$$\frac{d\sigma}{d\Omega} = \sum_n a_n \ \cos^n(\theta_{cm}) \quad , n = 0, 1, 2, ...$$

If only I=0 or I=1 contributes to the $\pi^{\pm}$ production, then the differential cross section should be symmetric about $\pi/2$ (i.e. involves only terms with even n's) because of charge symmetry considerations. On the other hand, if both I=0 and I=1 contribute, then asymmetry in the differential cross section will be present due to interference between the isoscalar and isovector amplitudes.

The earlier work done in the np channel by [Han65] indicated a large fraction of pion production came from I=0, while that of [Kaz67] indicated a smaller con-

tribution. However, these experiments lacked sufficient data, and thus a definite conclusion could not be drawn.

Lately, several kinematically incomplete experiments investigating the $NN\pi^{\pm}$ reactions have been conducted. Thomas *et al.* [Tho81] measured the differential cross sections for both positive and negative pions at angles $4^0 \leq \theta_{cm} \leq 113^0$, using a neutron beam ($T_n = 790\ MeV$) incident on a hydrogen target. No asymmetry in the differential cross section (i.e. no term in cos $(\theta_{cm})$) was found. However, small differences between the energy spectra of the $\pi^{\pm}$ were observed. These differences were attributed to a small contribution from the I=0 channel.

At SIN (Swiss Institute for Nuclear Research) Kleinschmidt et al. [Kle80] measured the differential cross section for $nn\pi^+$ at lower incident neutron energies (470 to 590 $MeV$) and angles $\theta_{lab} \leq 20^0$. A continuation of this work was reported by Fischer et.al. [Fis87] who measured both the $nn\pi^+$ and $pp\pi^-$ differential cross sections at the same neutron energies but at angles in the backward directions. These measurements found an appreciable contribution from I=0 ($\sim 40\%$). The anisotropy observed in the differential cross sections also seems to confirm this result. But these measurements were taken at only small angles, and hence their results can not be considered very reliable.

Another experiment which investigated this subject was that of Dakhno *et al.* [Dak82]. The $pp\pi^-$ cross section was measured using a proton beam (500 to 1000 $MeV$) incident on a deuterium bubble chamber. They found that the isoscalar cross section is close to zero for energies up to 750 $MeV$ and grows rapidly for energies higher than that.

The values of $\sigma_{11}$, that were used by the above experiments in the extraction of $\sigma_{01}$, were taken from old experiments which lacked sufficient accuracy. However, the recent measurements of the $pp \rightarrow pp\pi^0$ cross section by Didelez *et al.* [Did91]

and Andreev *et al.* [And88], who performed their experiments at the same incident neutron energies as [Kle80] and [Dak82] respectively, yielded very similar values for $\sigma_{01}$.

In the phase shift analysis by [Ver82], the isoscalar cross section $\sigma_{01}$ was found to be practically zero up to about 1 $GeV$, while in a similar analysis by [Bys87], $\sigma_{01}$ was found to be small but not negligible. Bystricky pointed out that even though the I=0 contribution to the cross sections might be small, it still plays an important role in spin observables. Unfortunately, at present, there are no published data on any of the spin observables in the np channel. Such a situation points out the need for accurate data, especially of the $np \rightarrow NN\pi^{\pm}$ reactions.

Two kinematically complete experiments, designed to measure the differential cross section and the analyzing powers for the $np \rightarrow pp\pi^-$ reaction, have already produced data; one at TRIUMF ($T_n = 440\ MeV$) (the subject of this thesis) and the other at Saturne ($T_n = 650\ MeV$). The Saturne measurement lies in the region where the $\Delta$ resonance is dominant, while the TRIUMF experiment's low energy minimizes this dominance; thus emphasizing the non-delta resonances [Dav91]. A third experiment at LAMPF intended to use both polarized beam and target, and a neutron energy $T_n = 790\ MeV$ has been cancelled.

## 1.4 Motivation

The motives behind carrying out this experiment to study the $np \rightarrow pp\pi^-$ include:

- This reaction possesses many important features, as pointed out in section (1.2), that make it a very valuable reaction for testing theories and learning more about the dynamics of NN interaction.

- At present, there are no kinematically complete data, nor are there any data for spin dependent observables for the $np \rightarrow pp\pi^-$ reaction. It is the objective of this experiment and the Saturne experiment to provide sufficient data to enable the performance of a phase shift analysis for this reaction.

- A unique feature of $np \rightarrow pp\pi^-$ is that its final state consists entirely of charged particles making the performance of a kinematically complete experiment relatively straightforward.

- There is still some inconsistency about the contribution of the isospin zero channel. Accurate measurements of the $np \rightarrow pp\pi^-$ reaction will help in solving this inconsistency.

# CHAPTER 2

## Experiment

The single pion production experiment $\vec{n}p \rightarrow pp\pi^-$ was performed using the neutron beam facility [Abe85] at the Tri-University Meson Facility (TRIUMF). The goal of this experiment was to measure the differential cross section ($\sigma$) and the three analyzing powers $A_{S0}$, $A_{N0}$ and $A_{L0}$ by scattering 438 MeV polarized neutrons from a liquid hydrogen target ($LH_2$) and detecting at least the two protons produced. Work on this experiment started in 1985, and final data taking was done in late 1990 and early 1991.

An optically pumped polarized ion source [Buc91], recently installed at TRIUMF (1990), was used to produce a 50% polarized proton beam with an intensity of 5$\mu$A (sec. 2.1.1). The proton beam was transported from the cyclotron to the $LD_2$ target via beamline 4A/2 (sec. 2.1.2). Two polarimeters (IBP and CSB), located upstream of the $LD_2$ target, measured the X and Y components of the polarization (sec. 2.1.3). A monitor of the time width of the beam burst was used in conjunction with a phase restricted cyclotron tune to reduce the time width of the proton burst to $< 0.5\ ns$ from its normal 3.8 $ns$. This apparatus was installed in one arm of the CSB polarimeter downstream of the polarimeter scintillators.

The 438 $MeV$ neutrons were produced in the $LD_2$ target via the D($\vec{p}$,$\vec{n}$)2p reaction (sec. 2.2.1). The polarized neutron beam was extracted at the $9^0$ port of a 3.37 $m$ lead collimator (sec. 2.2.2). Two spin precession magnets ("CLYDE" and "BONNIE"), located downstream of the collimator, rotated the spin of the neutrons to the desired direction ( normal(N), sideway(S), or longitudinal(L))

before they impinged on the $LH_2$ target (sec. 2.2.3). The polarization of the neutron beam was monitored by two neutron polarization monitors; one situated upstream of two spin precession dipoles, and the other downstream of the detection apparatus (sec. 2.2.4). A neutron profile monitor, located directly upstream of the second polarization monitor, was used to determine the position of the neutron beam.

The detection apparatus was designed to detect at least the two protons produced in the $np \rightarrow pp\pi^-$ reaction. It consists of a time of flight system (TOF) (sec. 2.3.1), drift and delay line chambers (sec. 2.3.2), and several small veto and position defining detectors (sec. 2.3.3).

## 2.1 Proton Beam

### 2.1.1 Production

A hydrogen plasma is created by microwave ionization of hydrogen gas in a magnetic field region. An electrode system extracts the proton beam from the hydrogen plasma and accelerates it to about 5 $keV$. The beam passes through a cell filled with polarized sodium vapor. The polarization of the vapor is produced by optical pumping of the sodium atoms with circularly polarized laser light tuned to the sodium $D_1$ transition. About a quarter of the incident 5 $keV$ protons are neutralized by picking up a polarized electron from the sodium and the rest of beam is removed by two deflector plates placed downstream of the neutralizer cell. The hydrogen atoms enter another cell filled with thick sodium vapor (40 to 80 $\times 10^{13}$ $atoms/cm^2$) where about 7% of them are ionized by picking up a second electron. In the region between the neutralizer and ionizer cells, the magnetic field reverses direction. At the zero crossing of the magnetic field, the parallel electron/proton

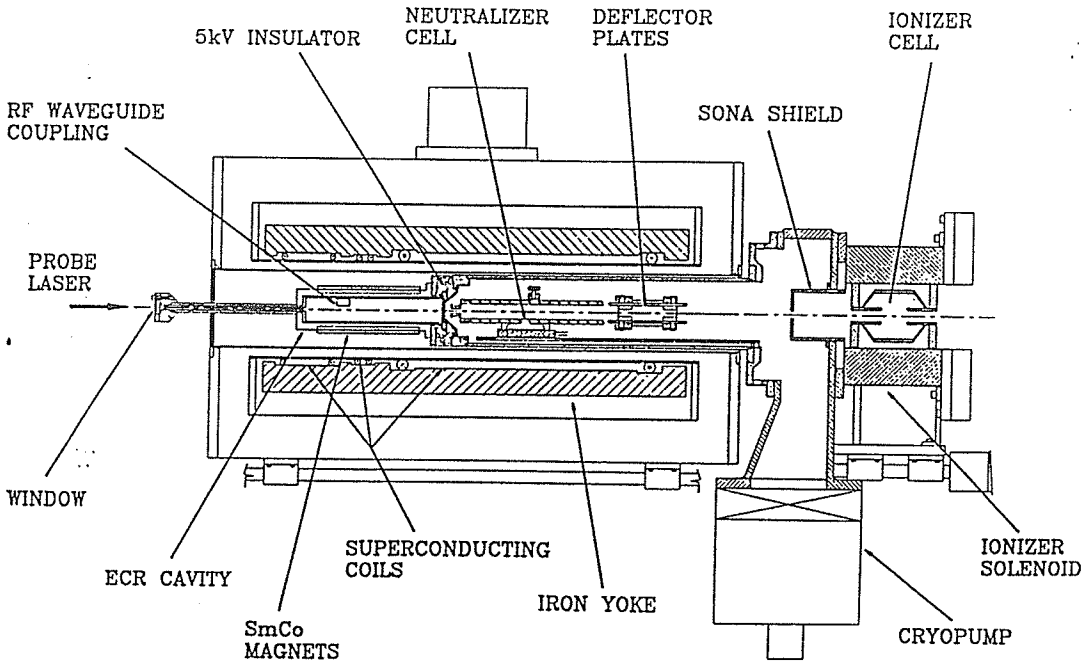


Figure 2.1: Schematic diagram of the ion source (from [Buc91]).

state remains almost the same, while the antiparallel state reverses its proton orientation, thus enhancing the proton polarization. A magnetic field transition of this type is called a *Sona transition.* The polarized $H^-$ beam is then accelerated to 300 keV and injected into the TRIUMF accelerator. A detailed description of the ion source and its operation can be found in reference [Buc91].

The TRIUMF accelerator is a sector focused cyclotron with six hills and valleys in the magnetic field. It accelerates the $H^-$ ions in a vacuum tank kept at $5 \times 10^{-8}$ *torr* or better [Mat87] to avoid beam loss by gas stripping. The proton beam is extracted by stripping the two electrons from the $H^-$ ions using a thin carbon foil placed at a radial position corresponding to the desired energy.

Under normal conditions the microscopic structure consists of a 3.8 *ns* beam pulse every 43 *ns*. For this experiment the 3.8 *ns* long beam bursts had to be

reduced to $< 0.5\ ns$ in order to get a better resolution of the time difference between the event trigger and the cyclotron rf and hence to be able to remove the low energy tail of the neutron beam.

A radial flag and up to four slits were used to intercept the $H^-$ ions which were not following the ideal path inside the cyclotron and hence restrict the phase width of the beam. The radial flag, which is made of pyrolytic graphite, was used to remove part of the beam in the first turn in the cyclotron, while the slits were inserted in the central region of the cyclotron (68 to 280 $cm$) to further reduce the width of the burst to about 0.5 $ns$ [Mat87]. The slits are made of tantalum plates.

In the phase restricted tuning about 90% of the proton beam was removed; this made the use of a high intensity producing ion source (such as the new ion source mentioned above) essential for the completion of the experiment.

### 2.1.2 Transport System

The layout of the beam transport system is shown in figure 2.2. The proton beam was transported from the cyclotron to the $LD_2$ target using dipole steering magnets (4VMC, 4VSM1, 4VB1, 4ASM2 and 4ASM3) and quadrupole focusing magnets (4VQ1, ...,4VQ7).

Several beam profile monitors (4AM3, ..., 4AM5) could be inserted in the beam line to monitor the beam spatial properties. In addition to determining the vertical and horizontal positions of the proton beam, signals from the two pairs of split-plate secondary emission monitors (4AM4.4 and 4AM4.7) were also used by a feed back system to calculate the desired corrections to the beam transport magnets, thus keeping the beam centroid stable to $< 0.2\ mm$ at the $LD_2$ target [Abe85].

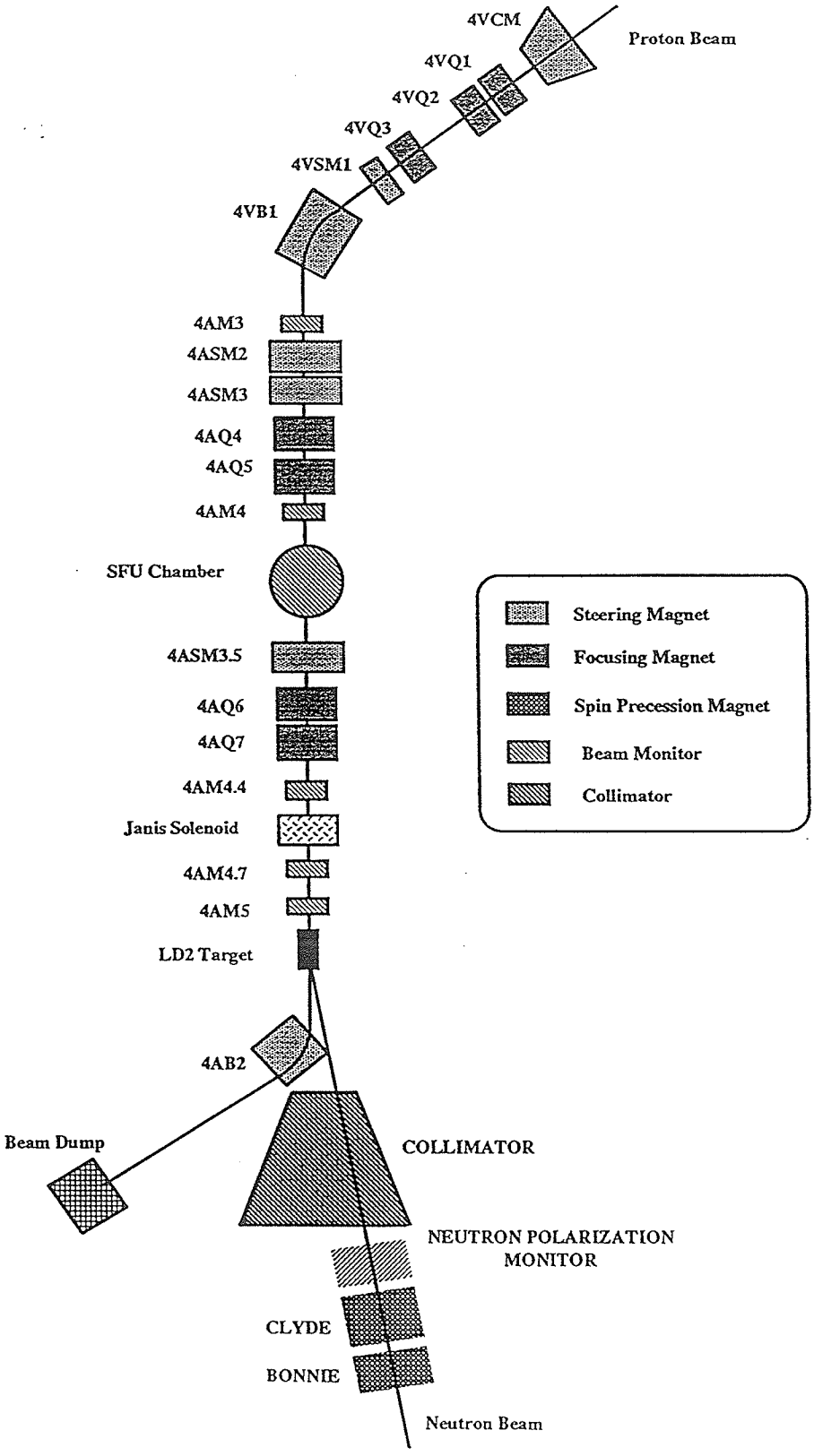


Figure 2.2: Layout of the beam transport system.

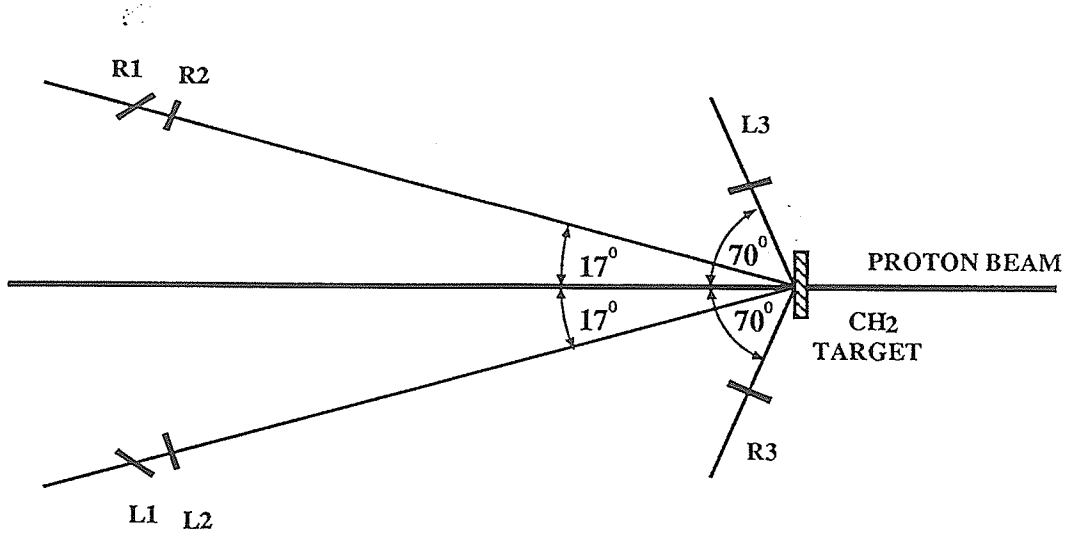


Figure 2.3: schematic diagram of the IBP left-right detectors.

### 2.1.3 Polarimeters

The polarization of the proton beam was determined by two polarimeters. One was installed in the SFU chamber, 5.8 $m$ upstream of the $LD_2$ target, and is referred to as the CSB polarimeter [Gre81]. The other polarimeter was stationed 7.2 $m$ upstream of the $LD_2$ target and is referred to as the In-Beam Polarimeter (IBP) [Abe87].

The IBP is a four arm polarimeter, with 2.8 $msr$ acceptance, capable of measuring the left-right and up-down asymmetries of the elastically scattered protons from the polyethylene $(CH_2)_n$ target (from here on the polyethylene $(CH_2)_n$ will be referred to as $(CH_2)$ ). Figure 2.3 illustrates the left-right detectors of the polarimeter. Each arm consists of three scintillators, C1 C2 and C3, where C can be R(right), L(left), U(up), or D(down). The C1 and C2 counters are placed at an

Table 2.1: Details of the left arm detectors for the IBP polarimeter.

| Description | C1 | C2 | C3 |
|---|---|---|---|
| Size $cm^3$ | $5.9 \times 5.1 \times 0.6$ | $5.1 \times 5.1 \times 0.6$ | $15.2 \times 5.1 \times 1.3$ |
| Distance to target | 76.2 $cm$ | 50.8 $cm$ | 20.3 $cm$ |
| Angle wrt beam | $17^0$ | $17^0$ | $70^0$ |
| Rotation angle | $37^0$ | - | - |

angle of $17^0$ (close to the angle of maximum analyzing power curve [Abe87]) to detect the forward scattered protons and C3 is placed at an angle of $70^0$ with respect to the proton beam to detect the associated recoil protons. Sizes of the scintillators counters and their distances from the $CH_2$ target are given in Table 2.1.

Shifts of the centroid of the proton beam change the solid angle and the p-p cross section. To make the polarimeter insensitive to small beam movements, the solid angle defining counter, C1, was rotated $37^0$ with respect to the scattered proton direction to account for the changes mentioned.

The second polarimeter, CSB, is very similar in design to the IBP polarimeter except that it has only two arms for measuring the vertical polarization of the proton beam and a much tighter geometry in order to minimize spurious (p,2p) events from $^{12}C$. The location of the polarimeter's target is adjusted along the beam axis according to the energy of the incident protons in order to compensate for changes in the opening angle between the scattered and recoil proton with energy. A layout of this polarimeter is shown in figure 2.4 and the design details are tabulated in table 2.2.

The system installed in the forward arm of the CSB polarimeter to monitor the width of the proton beam bursts is shown in figure 2.4. It consists of four small scintillators (TF1, TF2, TF3, and TF4) mounted on two Hamamatsu R1548

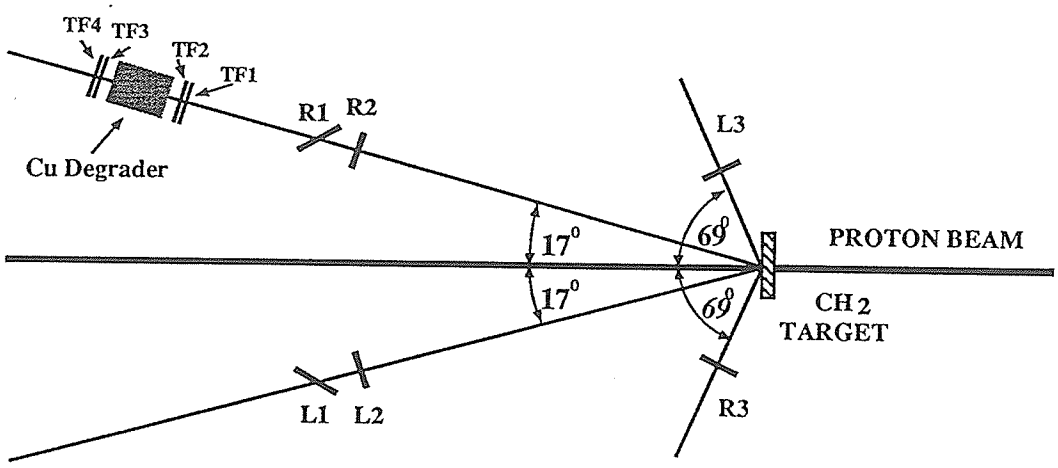


Figure 2.4: schematic diagram of the CSB polarimeter.

Table 2.2: CSB proton polarimeter specifications.

| Description | Solid Angle Defining Counter | Recoil Counter |
|---|---|---|
| Vertical dimension | 1.0 $cm$ | 2.0 $cm$ |
| Horizontal dimension | 2.5 $cm$ | 1.0 $cm$ |
| Distance to target | 77.47 $cm$ | 20.32 $cm$ |
| Solid angle | 0.16 $msr$ | 4.84 $msr$ |
| Angle wrt beam | $17^0$ | $68.9^0$ |
| Rotation angle | $68^0$ | - |

photomultiplier tubes (PMT's), each having two complete photocathodes, divider chains, and anodes within a common envelope. A Cu degrader was placed between the two PMT's to remove low energy particles produced in the polarimeter's kapton [1] foil.

The width of the beam bursts was determined by requiring the TF1.TF3 coincidence and timing the rf against TF1. The resolution of the PMT's was attained by timing signals from the anodes of the same PMT against each other. An overall resolution of the system of 110 $ps$ full width at half maximum (FWHM) was achieved [Dav90].

## 2.2 Neutron Beam

### 2.2.1 Production

The 438 MeV polarized neutron beam used for this experiment was produced in the liquid deuterium ($LD_2$) target via the D($\vec{p}$,$\vec{n}$)2p reaction. The $LD_2$ target cell was 19.7 $cm$ long and 5 $cm$ in diameter, with 0.25 $mm$ stainless steel walls and 0.051 $mm$ stainless steel end windows [Abe85].

The angular distribution of the Wolfenstein polarization transfer parameters ($D_t$, $R_t$, $R_t'$, $A_t$,and $A_t'$) [Hos68] for free p-n scattering with $T_p$= 460 $MeV$ is shown in figure 2.5. For neutrons produced via the quasielastic reaction D($\vec{p}$,$\vec{n}$)2p, the Wolfenstein parameters are subject to small corrections (of a few percent) due to final state interactions [Bug87], and they are denoted by small letters such as $r_t$, $r_t'$, etc. As can be seen from the graphs of figure 2.5, the "$R_t$ mechanism" (i.e. the polarization of the incident protons is in the horizontal direction and the neutrons are extracted at an angle of about $9^0$) is the best method of attaining

[1] Dupount Corporation

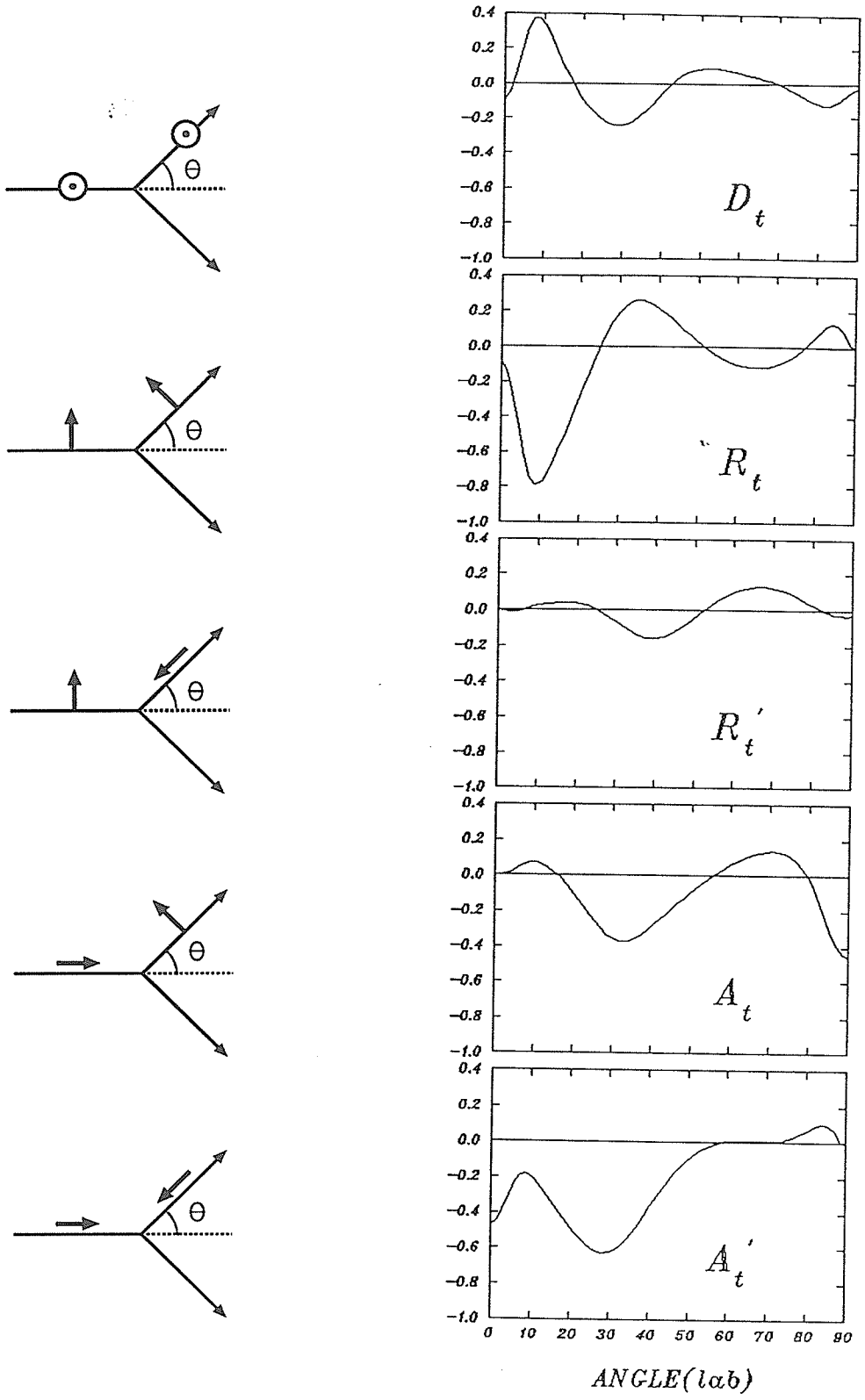


Figure 2.5: Definitions of the Wolfenstein polarization transfer parameters and their angular distribution for for incident protons of 460 $MeV$.

the maximum possible neutron polarization.

A spin precession solenoid "JANIS", located 1.8 $m$ upstream of the $LD_2$ target, was used to process the initially vertical proton polarization into the transverse direction. The neutrons produced in the $LD_2$ target were extracted at the $9^0$ angle with a polarization direction almost exactly opposite to that of the protons ( the nonzero values of $r_t'$ and $P$ at $9^0$ resulted in small components of the neutron polarization in the $L$ and $N$ directions respectively, see figure 2.6 ). The primary proton beam was removed from the neutron beam by a sweeping magnet placed directly downstream of the $LD_2$ target.

### 2.2.2 Collimation

The neutron beam was brought down through a 3.37 $m$ long collimator constructed of steel pipes welded to a steel frame filled with lead. The pipes were built in two sections, the upstream section was 1.87 $m$ long and 10.2 $cm$ in diameter while the downstream section was 1.5 $m$ long and 12.8 $cm$ in diameter. Eleven 30.5 $cm$ long cylindrical steel collimators were inserted in the $9^0$ part to define the neutron beam profile. The steel collimators had rectangular apertures ranging in size from $39.1 \times 18.6\ mm^2$ upstream to $46.1 \times 32.2\ mm^2$ downstream. The entrance of this collimator was 2.87 $m$ downstream of the $LD_2$ target center.

To reduce the flux of neutrons that had scattered from the walls of the first collimator, another collimation system was placed within the pole faces of the dipole magnet "CLYDE". It was constructed by stacking lead bricks forming a 0.61 $m$ thick collimator with a 51.3 $mm$ by 50.8 $mm$ aperture.

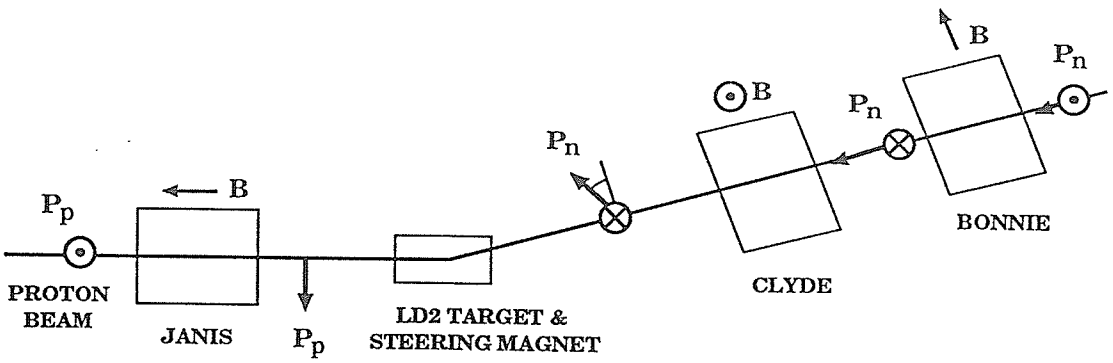


Figure 2.6: Polarization transfer and spin rotation in producing vertically polarized neutrons (in this case all the three spin precession magnets are used).

### 2.2.3 Spin Precession

Two spin precession dipole magnets, CLYDE and BONNIE, placed between the main collimator and the $LH_2$ target, rotated the spin of the neutrons to the desired direction (N, S, or L).

To rotate the polarization of the neutrons into the desired L or S direction, only the first dipole magnet CLYDE, which has a vertical magnetic field, was used. The polarization of the neutrons was already rotated by $26^0$ due to the nonzero value of $r_t'$ and to the fringe field of the steering magnet, hence, only a net rotation of $64^0$ or $-26^0$ was required to obtain a polarization in the L or S direction respectively. This was done by setting the polarity and current of CLYDE to the correct values. In the case of rotation to the vertical direction, both dipole magnets were employed in which CLYDE rotated the polarization in the L direction and BONNIE, with a horizontal field, rotated the polarization into the N direction. A schematic diagram of the precession of the neutrons' polarization through the magnets is shown in figure 2.6.

The dipole magnet CLYDE was calibrated by turning off BONNIE and finding

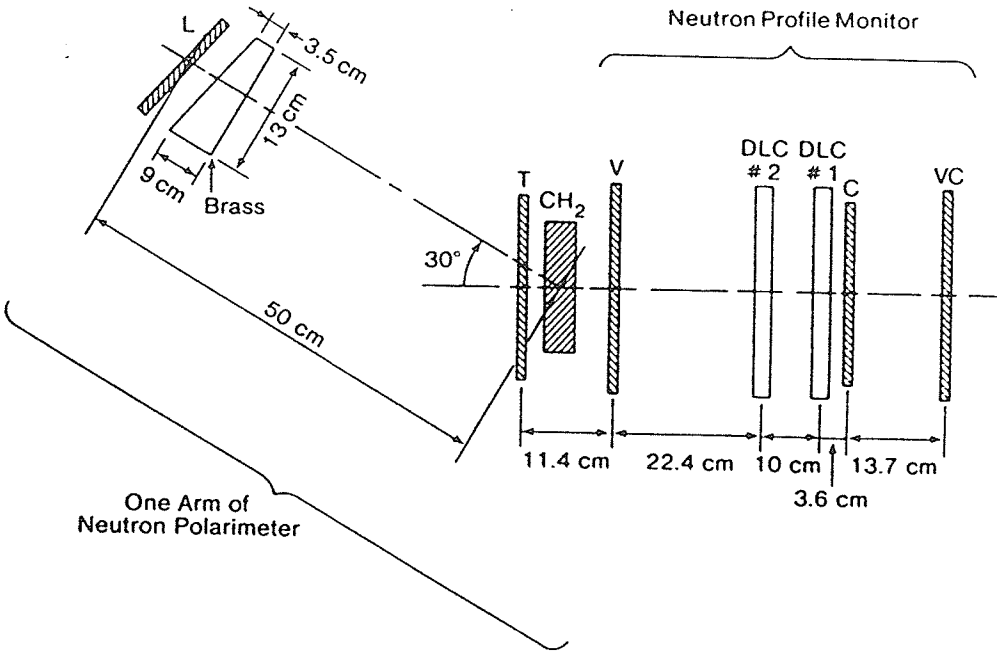


Figure 2.7: Schematic diagram of the neutron beam profile monitor and one arm of the neutron polarimeter (from [Abe85]).

the zero crossing of the up-down asymmetries in the neutron polarimeter, while the dipole magnet BONNIE was calibrated by turning off the superconducting solenoid JANIS and determining the zero crossing of the left-right asymmetries. Both magnets were monitored during the course of the experiment by NMR probes.

### 2.2.4 Neutron Beam Profile And Polarization Monitors

A neutron beam profile monitor, capable of determining the position of the centroid of the neutron beam to within $\pm 0.5\ mm$, is located 4.3 $m$ downstream of the $LH_2$ target in the $9^0$ port. A schematic diagram of the beam profile monitor is shown in figure 2.7. It consists of a veto scintillator (VC) to reject charged particles in the neutron beam, a converter scintillator (C) to produce protons via n-p elastic scattering and two $20.3 \times 20.3\ cm^2$ delay line chambers to track back

the knocked out protons. The vertical and horizontal beam profiles were obtained by tracing back the proton trajectories to the converter. Figure 2.8 shows some of the results obtained by this monitor.

The polarization of the neutron beam was monitored during the experiment by two neutron polarization monitors, one stationed between the main neutron collimator and the neutron spin precession dipole CLYDE (see figure 2.2) and the other located downstream of the neutron beam profile monitor. Due to the fact that the two monitors were not calibrated to measure exactly the neutron beam polarization, they were used in this experiment only to measure the ratio of the X and Y components of the neutron beam polarization. These ratios, along with the X and Y components of the proton polarization, can be used to deduce the Z component of the polarization.

Figure 2.7 shows the downstream polarization monitor. It consists of a 3.2 $mm$ thick veto scintillator (V) to reject charged particles, a 50 $mm$ thick ($CH_2$) target, a scintillator (T) to ensure that protons detected were produced in the $CH_2$ target and four identical 6.4 $mm$ thick scintillators each preceded by a wedge shaped brass absorber to correct for the proton energy spread and to remove low energy protons. The four scintillators were arranged in two branches, left-right and up-down. They subtended a solid angle of 175 msr around an angle of $30^0$ to the beam axis as measured from the center of $CH_2$ target. The measured analysing powers are $A_n^{eff}$(UD)=0.215 and $A_n^{eff}$(LR)=0.209. The upstream polarization monitor is very similar in design to the downstream one except that it is smaller due to space constraints.

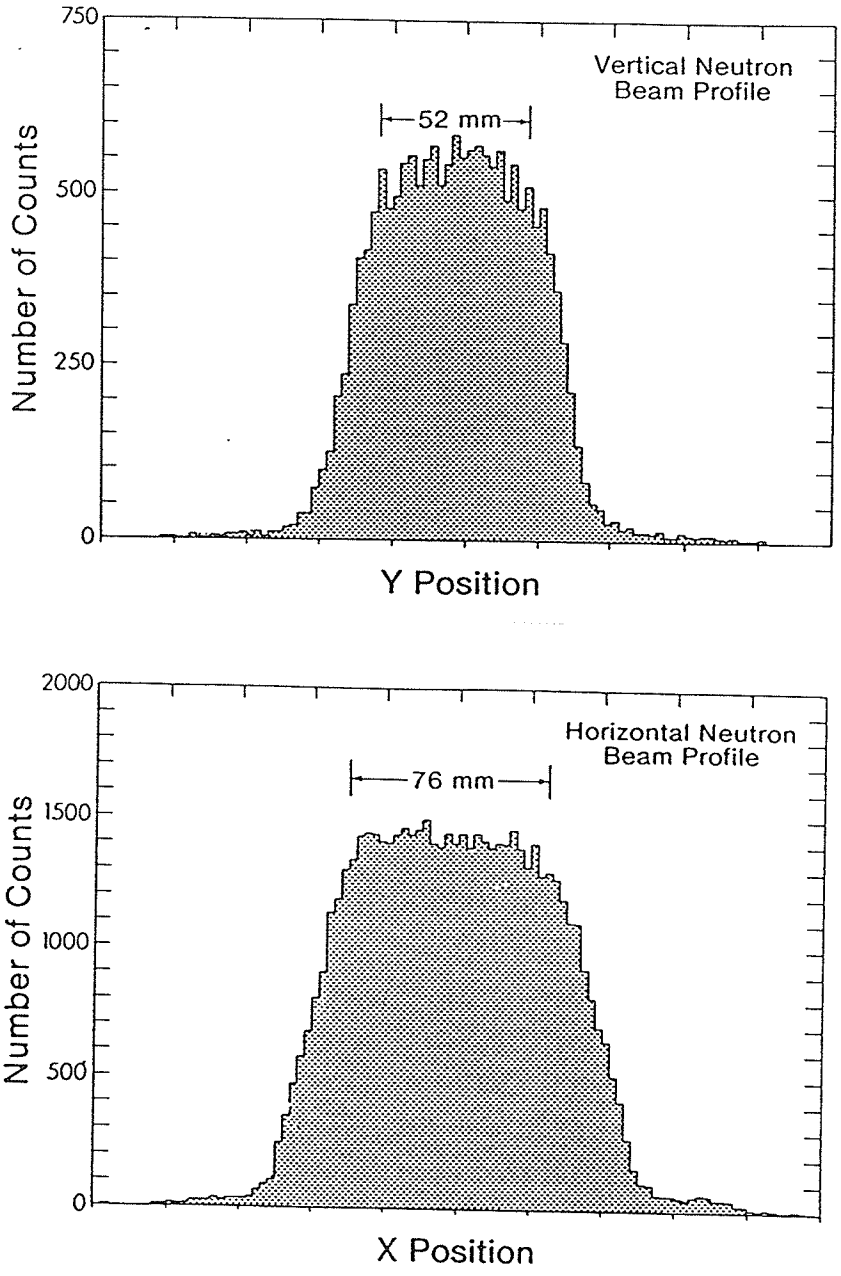


Figure 2.8: The vertical and horizontal neutron beam profiles at the profile monitor converter (from [Abe85]).

## 2.3 Detection Apparatus

A schematic diagram of the $LH_2$ target and the detection apparatus is given in figure 2.9. The $LH_2$ target was an upright mylar [2] cylinder 12.7 $\mu m$ thick, 16 $cm$ high and 5 $cm$ in diameter contained in an evacuated vessel. The vacuum vessel had large windows (23 $cm$ in diameter) made of 12.7 $\mu m$ kapton supported by 12.7 $\mu m$ kevlar cloth. The large window in the forward direction allowed particles with angles of up to $45^0$ for particles produced anywhere in the active volume of the target, and up to $60^0$ for particles produced at the center of the $LH_2$ target, to exit the vacuum vessel without any obstruction from its support or service structures.

The detection apparatus was designed to allow for the detection of at least the two protons produced in the np $\rightarrow$ pp$\pi^-$ reaction. The two protons were kinematically restricted to exit within the area covered by the forward apparatus, but the pion could be emitted anywhere.

To specify a reaction with three bodies in the final state, at least five observables should be measured. In this experiment, a TOF system and two drift chambers were used to measure at least six observables (the energy and the angles of each proton). If the pion was also detected in the forward direction, then the reaction is over determined.

### 2.3.1 Time Of Flight

The time of flight (TOF) system was constructed to fulfill two purposes: (i) to determine the energy of the two protons and that of the pion if it exited in the the forward direction and (ii) to serve as part of the trigger.

[2] Dupount Corporation

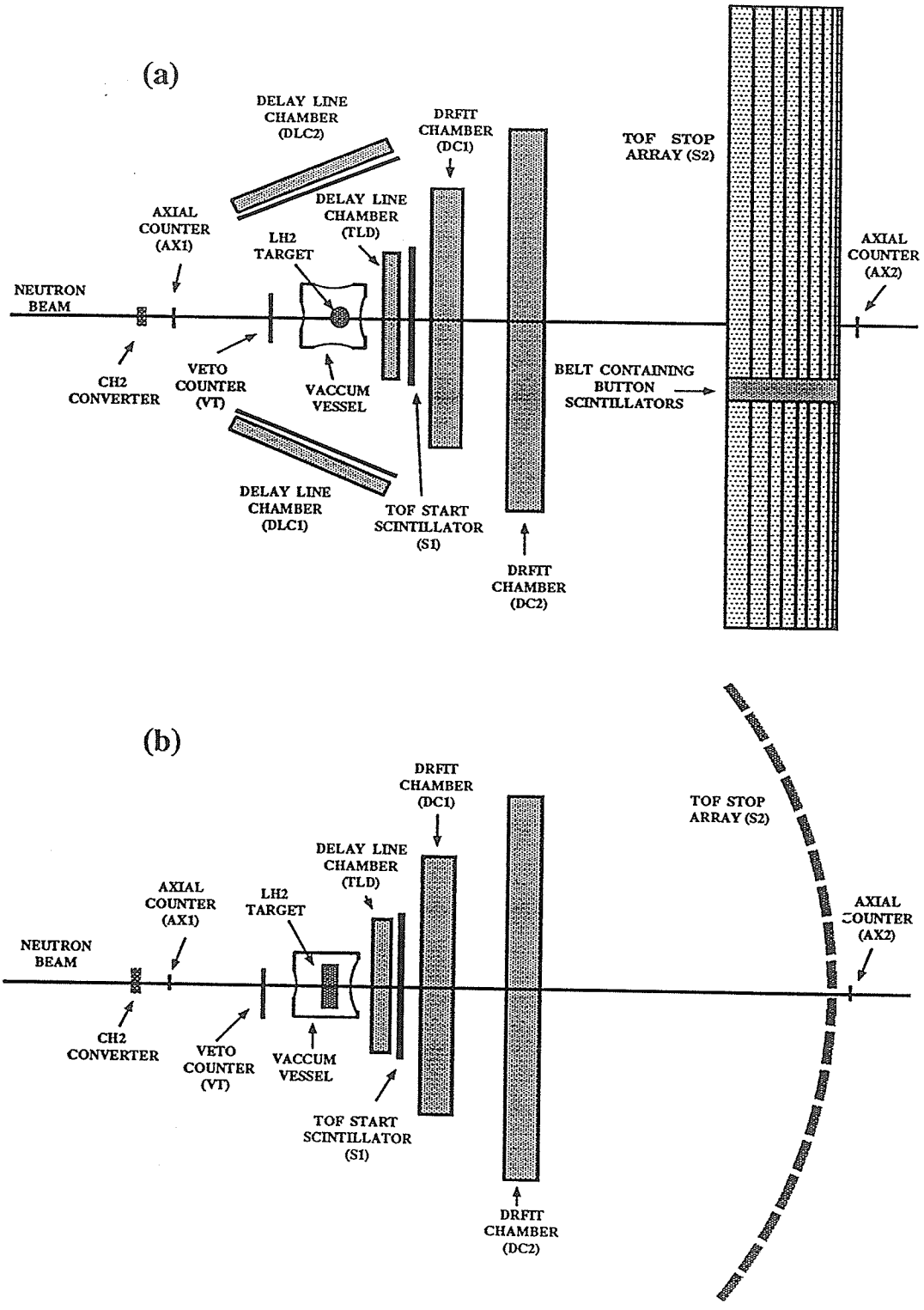


Figure 2.9: Schematic diagram of the detection apparatus: (a) top view, (b) side view.

Table 2.3: Dimensions of the TOF scintillators.

| Scintillator number | | Length $[cm]$ | Width $[cm]$ | Thickness $[cm]$ |
|---|---|---|---|---|
| S1 | | 30 | 30 | 0.6 |
| S2 | 2 | 200 | 10 | 2 |
| | $3 \cdots 17$ | 200 | 10 | 3 |
| | 18 | 200 | 10 | 2 |
| | 19 | 200 | 10 | 1.9 |

The TOF system consisted of a start scintillator (S1), placed 15 $cm$ downstream of the center of the $LH_2$ target, and a stop scintillator (S2) consisting of 18 bars of BICRON-408 [3] assembled in a cylindrical array. The axis of the (120 $cm$ radius) cylindrical array was horizontal and passed through the center of the $LH_2$ target. The reason for this configuration was to reduce the probability of a single particle hitting two adjacent bars. Table 2.3 gives the dimensions of the TOF scintillators.

The S1 and S2 bars were viewed by two photomultiplier tubes (PMT's) connected to them via light guides. Signals from these PMT's were fed to time-to-digital converters (TDC) and to analog-to-digital converters (ADC). The mean time of the two PMT's for S1 was also available.

[3]Bicron Corporation, 12345 Kinsman Road, Newbury, Ohio

### 2.3.2 Drift and Delay Line Chambers

#### Drift Chambers

Two drift chambers (DC1 and DC2), with active areas of $50 \times 100\ cm^2$ and $100 \times 150\ cm^2$, respectively, were placed between TOF start scintillator S1 and TOF stop scintillator S2. They were used to determine the trajectories of the two protons and that of the pion if it went through them.

Each drift chamber (DC) consists of two protective covers made of 2.54 $\mu m$ aluminized mylar and six wire planes, each sandwiched between two high voltage (HV) planes made of 2.54 $\mu m$ aluminized mylar and maintained at about -2200 volts. The distance between each wire plane and the HV planes is 1.35 $cm$.

The wire planes are arranged in the sequence UYXXUY, where the U plane is at $45^0$ to the X and Y planes. Every wire plane consists of sense wires made of 2.54 $\mu m$ gold plated tungsten situated between two field forming wires made of 20.32 $\mu m$ stainless steel and set at about -3300 volts. The distance between each sense wire and field forming wires is 2.54 $cm$.

A gas mixture of about 4% alcohol and equal amounts of argon and ethane, flowed continuously through the DCs at a pressure that counter-balances the electrostatic attraction between the anode and cathode planes.

A LeCroy 4290 wire chamber readout system was used to read out pulses produced on the wires. It consists of an amplifier/discriminator card, 32 channel TDC units and the 4298 system controller.

#### Delay Line Chambers

In the $np \rightarrow pp\pi^-$ reaction, only pions could scatter in the backward direction. In order to detect large angle pions for calibration purposes, two delay line chambers (DLC1 and DLC2), each preceded by a scintillator counter, were placed on the

sides of the $LH_2$ target (see figure 2.9).

### 2.3.3 Veto and Position Defining Detectors

#### Veto Detectors

In order to reduce the background, a veto scintillator (VT) and a delayline chamber "Thin Logic Device" (TLD) were used and required as part of the trigger. The VT was positioned 26 $cm$ upstream of the $LH_2$ target to reject charged particles in the neutron beam. The TLD was placed directly in front of S1 as a low mass device. It was not used for tracking particles; it was used only to signal the passage of a charged particle through it and hence cut down the background arising from the interaction of the neutron beam with S1.

#### Position Defining Detectors

Two tiny ($1 \times 1$ $cm^2$) scintillators AX1 (16 $cm$ upstream of VT) and AX2 (directly downstream of S2) and a $CH_2$ converter to produce recoil protons were inserted in the neutron beam to define a "pencil beam" of protons. The pencil beam could later be used to determine the absolute orientation and position of the drift chambers by relating the trajectories measured in them to the beam axis as defined by the axial scintillators.

A set of small scintillators ($5 \times 5$ $cm^2$) was placed behind each S2 bar with their centers at x = -20 $cm$. Since these "button" scintillators were small and of well known position, they served as a known reference for calibration and monitoring the performance of the TOF system (see sections 3.3, and 3.4). The button scintillators were mounted in a single light guide belt which was viewed by two PMT's.

## 2.4 Data Acquisition

### 2.4.1 Electronics

The electronics diagrams for the detection system, excluding the drift chambers and delay line chambers, are shown in figures 2.10, and 2.11. The anode signal of each PMT connected to a TOF scintillator was split into two parts. The first was delayed and directed to an ADC module to be used for charge measurement. The second was fed into a constant fraction discriminator which generated two logic signals; one used as an input to a TDC module to be used for timing measurements, and the other was used for the determination of the trigger.

The electronics were designed to identify the following types of events:

- $np \rightarrow pp\pi^-$ events: to define potential $np \rightarrow pp\pi^-$ events, two triggers were used. The first was established by any PMT in the S2 array firing in coincidence with S1 and anti-coincidence with V (charged particle veto). This trigger sets the latch, starts TDC clocks, opens ADC gates, and strobes DCR units. In addition, it sets a FAST CLEAR signal which, unless suppressed by a higher level trigger signalling an acceptable event, will reset the TDC's, ADC's, and DCR's after a delay of 2 $\mu s$, so that they will be ready to accept the next event. The second level trigger was formed by requiring the following:

  1. The passage of a charged particle through the TLD.
  2. The firing of both PMT's of S1.
  3. The hitting of two bars, which due to kinematic constraints on the position, should be two outer bars (one from bars 2 to 8, and the other from bars 13 to 19) or two inner bars (9 to 12). This ensures that the

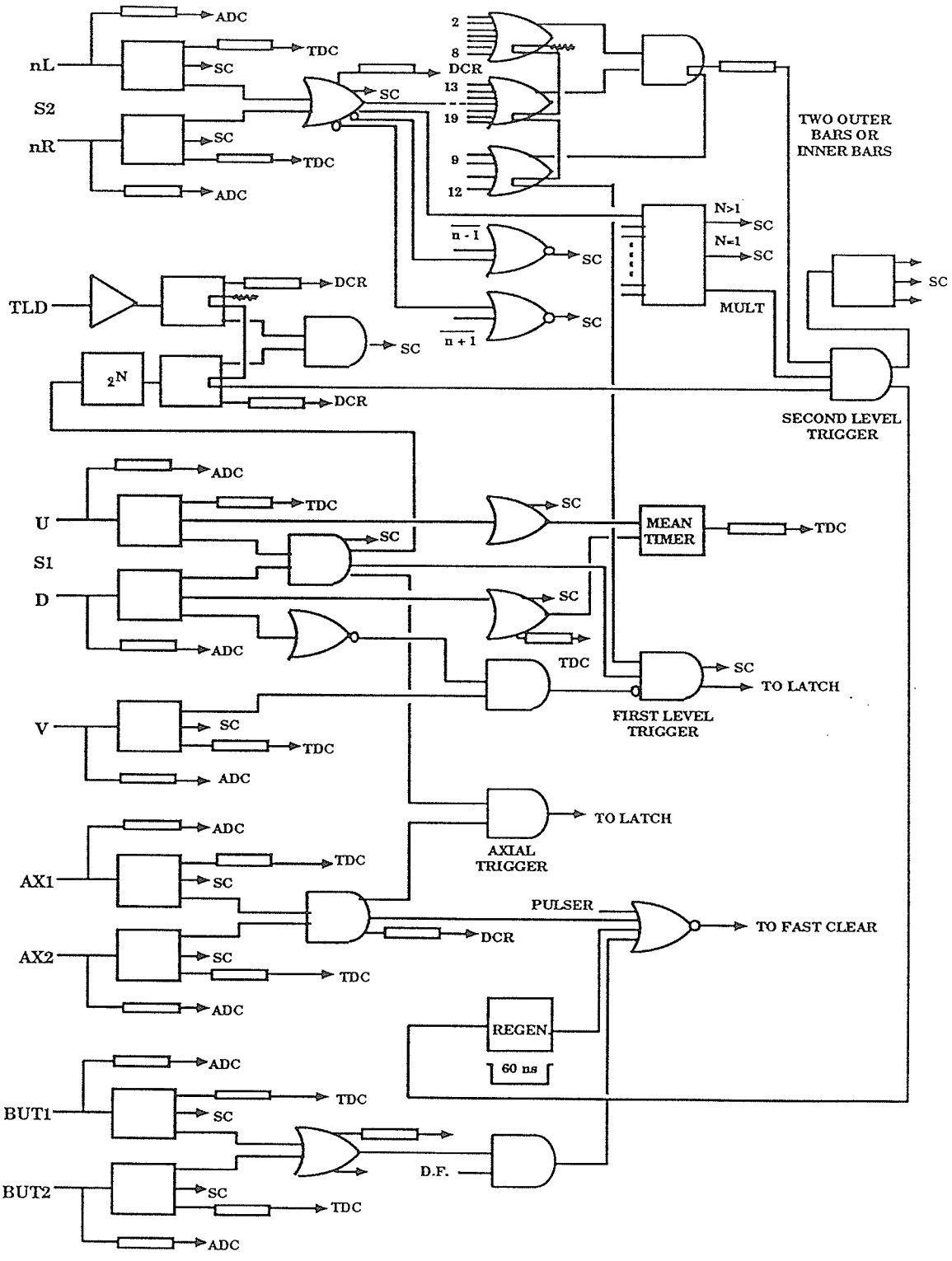


Figure 2.10: Electronics diagram # 1.

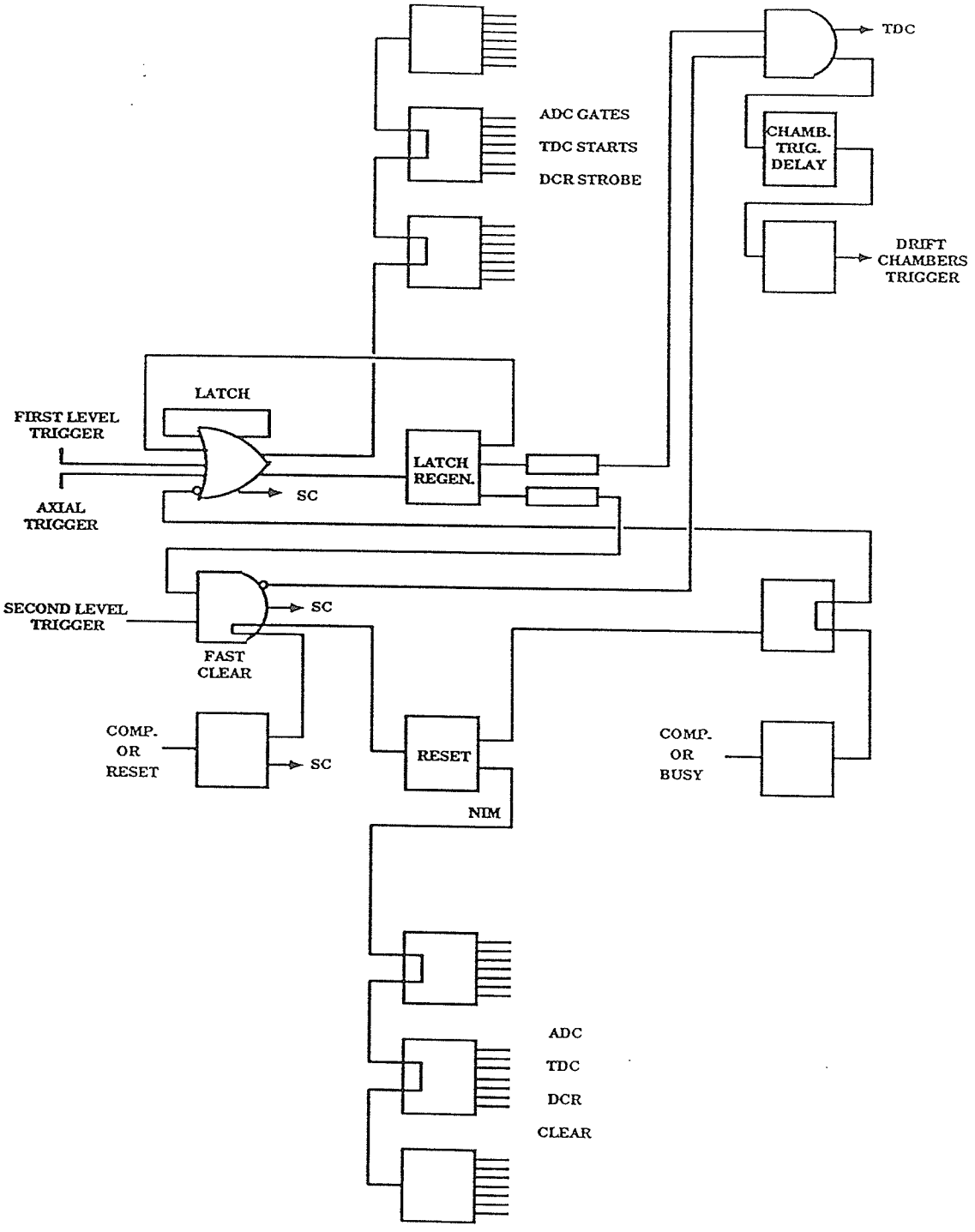


Figure 2.11: Electronics diagram # 2.

kinematic conditions on the two protons from an $np \rightarrow pp\pi^-$ reaction were met.

- $np \rightarrow np$ events: about 5% of the data taken were $np$ elastic scattering data which were mainly used for calibration purposes (see sections 3.4, and 3.5). The triggers that defined these events were the same as the ones used above, except that only one bar was required to fire for $np$ events instead of two for $pp\pi^-$ events.

- Button events: button events were obtained when a particle hit one of the small scintillators placed behind each S2 scintillator bar. To define these events, the firing of at least one of the two PMT's viewing the light guide belt that contained the button scintillators was also needed.

- Axial events: axial events were obtained when a proton produced from the $CH_2$ converter passed through both the AX1 and AX2 scintillators. The trigger for these events was established by requiring the firing of the two axial counters in coincidence with S1.

### 2.4.2 Data Collection and On-line monitoring

Whenever an event was correctly defined by the logic triggers, CAMAC registers would be read to a STARBURST module (referred to as J11). This module would perform checks on the data to ensure that a sufficient number of drift chamber wires had fired, but that an excessive number had not fired. In addition, it identified events as being due to neutrons or $\gamma$ rays on the basis of the time of the trigger with respect to the rf. Only some of the $\gamma$ ray events were retained whereas all neutron induced events were kept. If the checks were passed, the event would be stored in an event buffer. The J11 would continue processing events

until its 8 k memory was full; at that point it would send the data to the main data acquisition computer to be written to tape using a program called VDACS ( VAX Data ACquisition System) running in a background mode.

The events written to tape were of four different types:

- Event type 1 contained the information on about 210 scalers. It was a "clock event" read every 30 seconds.
- Event type 2 was a properly triggered event which contained all the TDC, ADC, DCR, and DC information.
- Event type 3 contained the information of an event triggered by the neutron beam profile monitor.
- Event type 5 was a self check event, where all CAMAC registers were set to 1 and read back.

On-line monitoring was done by a histogramming program called LISA. This program allowed the monitoring of performance of the different detectors used in this experiment. Some of the histograms and two dimensional plots that were defined and continually monitored were:

- A two dimensional plot to monitor the functioning of all the TDC and ADC units. It had the channel numbers on the x-axis and the word numbers in the event buffer on the y-axis.
- A histogram of the number of S2 bars that were hit per event.
- A histogram of the number of wires that fired in each DC.
- A histogram of the time of the event with respect to rf.

# CHAPTER 3

# CALIBRATION

The objective of this thesis is to calibrate the TOF system used in TRIUMF experiment (E372) to study single pion production from the $np \rightarrow pp\pi^-$ reaction. The calibration is concerned with: first, the determination of constants which would enable the calculation of the absolute values of:

- Impact position (section 3.3)
- Time Of Flight (section 3.4)
- Energy Deposited (section 3.5)

and second, the monitoring of the stability of these calibration constants through the whole course of the experiment.

As mentioned in the previous chapter, the detection apparatus used in the PIPROD experiment consists of two major systems: the TOF system and the drift chambers system. The drift chambers were used to provide information on the trajectories followed by charged particles, and these trajectories could be used to determine accurate impact positions of the charged particles on the TOF stop scintillators, thus, providing a method of checking the impact positions calculated from the scintillators alone. A cross-check with the drift chambers data was carried out to ensure that there was no bias between the two systems. Since the coding of the drift chambers was a major effort within the experiment undertaken by other members of the collaboration, the drift chamber data do not form part of the body of this thesis.

The TOF system calibration was carried out at the University of Manitoba using the physics VAX cluster. A program called BACCHUS with user written subroutines was used to read the data, identify good events, calculate needed variables and their corrections, and output results. A graphing software program called PLOTDATA [Chu90] was also used in histogramming, plotting, and/or fitting of some of the results. Information about NN scattering was provided by a program called SAID [Arn90].

## 3.1 Principle of scintillator-photomultiplier system

Plastic scintillators are one of the most widely used particle detectors in physics because of their fast decay time and their availability in different sizes. The principle of their operation [Bir64,Kno89] is that when a particle passes through a scintillator, a fraction of the kinetic energy lost by that particle is used to excite molecules of the scintillation material into higher energy levels. Most of this excitation energy is converted quickly to heat and lattice vibration, while a small fraction is given up in the form of light. The fraction of incident particle energy that is converted to light is referred to as the *scintillation efficiency*, and processes in which no light is produced are referred to as *quenching processes.*

Light is emitted isotropically from the track of an ionizing particle. As the light propagates inside a scintillator, two effects result in its attenuation. The first is scattering at surfaces of the scintillator. When the light strikes a surface two situations occur. If the angle of incidence $\alpha$ is greater than the critical angle $\alpha_c$ then the light will be totally reflected, and if $\alpha$ is smaller than $\alpha_c$ then only partial reflection will occur and therefore some of the light will be lost. Local conditions at the surface (minute cracks, *crazing*, due to age and mishandling) can result in an angle that is smaller than $\alpha_c$ and hence reduce the efficiency of light collection.

The critical angle $\alpha_c$ is defined as

$$\alpha_c = sin^{-1}\frac{n_1}{n_0}$$

where $n_0(n_1)$ is the index of refraction for the scintillator (air).

The second effect in which light is attenuated is absorption. In absorption some of the light gets absorbed by exiting molecules which then deexcite through quenching. Light with short wavelengths is strongly absorbed, and is totally lost after only short distances of travel inside a scintillator. In long scintillators, absorption is very important and a correction for this effect is given in section 3.5.

The speed of a light pulse inside a scintillator is given by

$$v = c/n \tag{3.1}$$

where $c$ is the speed of light, $n$ is the index of refraction for a scintillator. Often, a light pulse goes through several reflections before reaching the photomultiplier. Hence the speed with which a light pulse moves from the track position to the photomultiplier is given by the effective speed $V_{eff}$. The $V_{eff}$ is determined by the speed of light in the scintillator and the average path length that light traverses in that scintillator.

In most cases, the shape of the cross section of a scintillator does not match that of the photocathode of a PMT. To couple the two cross sections, light guides, which are typically constructed from transparent material that has a high index of refraction in order to minimize the critical angle and thus to optimize the collection of light, are utilized. Light guides are also used to filter out the short-wavelength light produced close to the end of a scintillator.

When light falls upon a photocathode, some of the photons are absorbed and cause the emission of electrons. The ratio of the number of photoelectrons produced to the number of incident photons is called the *quantum efficiency*. It ranges

for most PMTs from 20% to 30%. The photoelectrons are then accelerated and focused onto a structure called a dynode. For each electron striking the dynode, several other electrons are emitted. This process of secondary emission of electrons is repeated for several more dynodes, each held at a positive potential with respect the previous one. Millions of electrons are produced at the end of the multiplication for each photoelectron. These electrons are collected at the anode giving a fast electronic pulse which can be used for triggering and timing applications.

The time it takes the photoelectrons to travel from the cathode to the anode is called the "*electron transit time*". It ranges for most commercial PMTs from 20 to 80 *ns*. Two factors contribute to the spread of the electron transit time or "*time jitter*". The first is the spread of velocities of the photoelectrons due to the variation of the photons' wave lengths. The second is the variation of photoelectron path lengths from the point of emission at the cathode to the first dynode and the variation of path lengths of the electrons as they proceed down the dynode chain.

The number of electrons collected at the anode is directly proportional to the number of photoelectrons and varies as a function of the high voltage applied between the dynodes. In the case of large numbers of photoelectrons, disproportionality, or "*nonlinearity*", can arise because of space charge in the last stages of multiplication. This effect alters the trajectories of electrons and hence causes the loss of some electrons.

Spurious pulses, or "*noise*", are often produced at the anode of a PMT due to thermionic emission of electrons from the photocathode, Cerenkov processes in the glass of the PMT, and positive ions produced from the ionization of residual gases which make it back to the photocathode and initiate a random pulse. However, these pulses are usually small, since they are the result of a single photoelectron,

and they can easily be avoided by setting thresholds on the PMT pulse amplitude.

## 3.2 General description of the TOF system

The 18 scintillator bars, which constituted the TOF array, were made of BC408. The major characteristics of BC408 scintillators are given in table 3.1 [Hur85]. Each scintillator was loosely wrapped with thin aluminum foils to reflect back any scintillation light that escapes at angles less than the critical angle, a study of the effects of various outer reflector arrangements is given in reference [Dag81]. To the scintillators from outside light, each scintillator was covered with black paper and tape. Twisted lucite light guides were glued to the ends of each scintillator bar. Photographs of these light guides and the TOF array are shown in figure 3.1.

Each scintillator was viewed from both ends by a pair of XP2230 Photomultipliers. Signals from the PMTs were used to stop the clocks in the LeCroy 2228A TDC units (1024 channels, 50 $ps/ch$). As seen in figure 3.2, the times (in $ns$) at which signals from the left (L) and right (R) photomultipliers trigger the electron-

Table 3.1: Specifications of the BC-408 scintillator

| | |
|---|---|
| Light output (% anthrazene) | 64 |
| Decay time $[ns]$ | 2.1 |
| Wave length of max. emission $[nm]$ | 425 |
| H/C ratio | 1.104 |
| Density $[g/cm^3]$ | 1.032 |
| Refraction index | 1.58 |

(a)

(b)

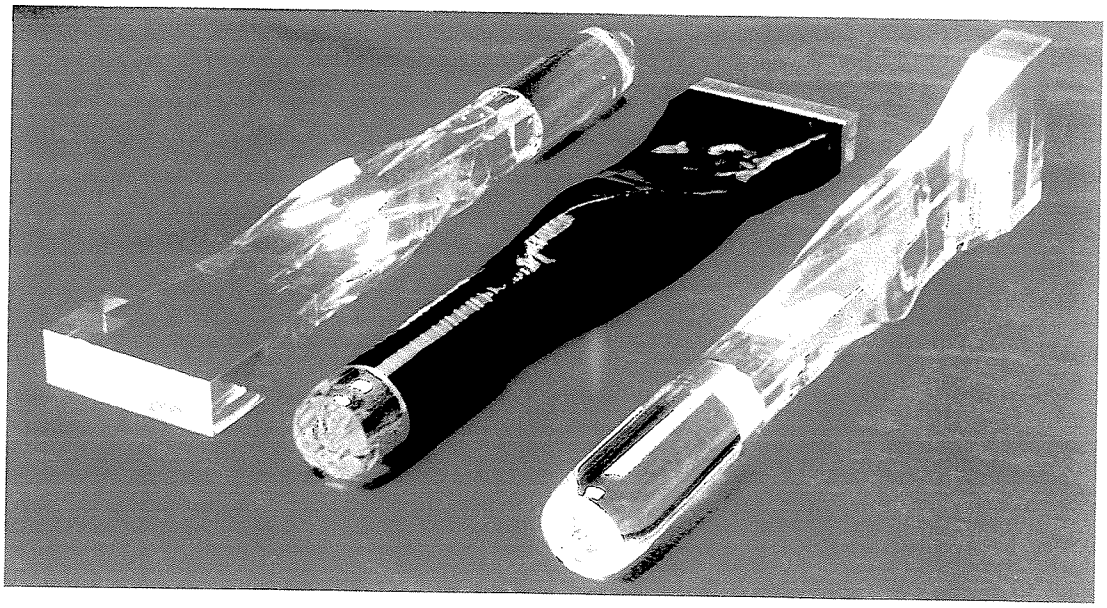

Figure 3.1: (a)Picture of the TOF stop array. (b)Picture of the light guides

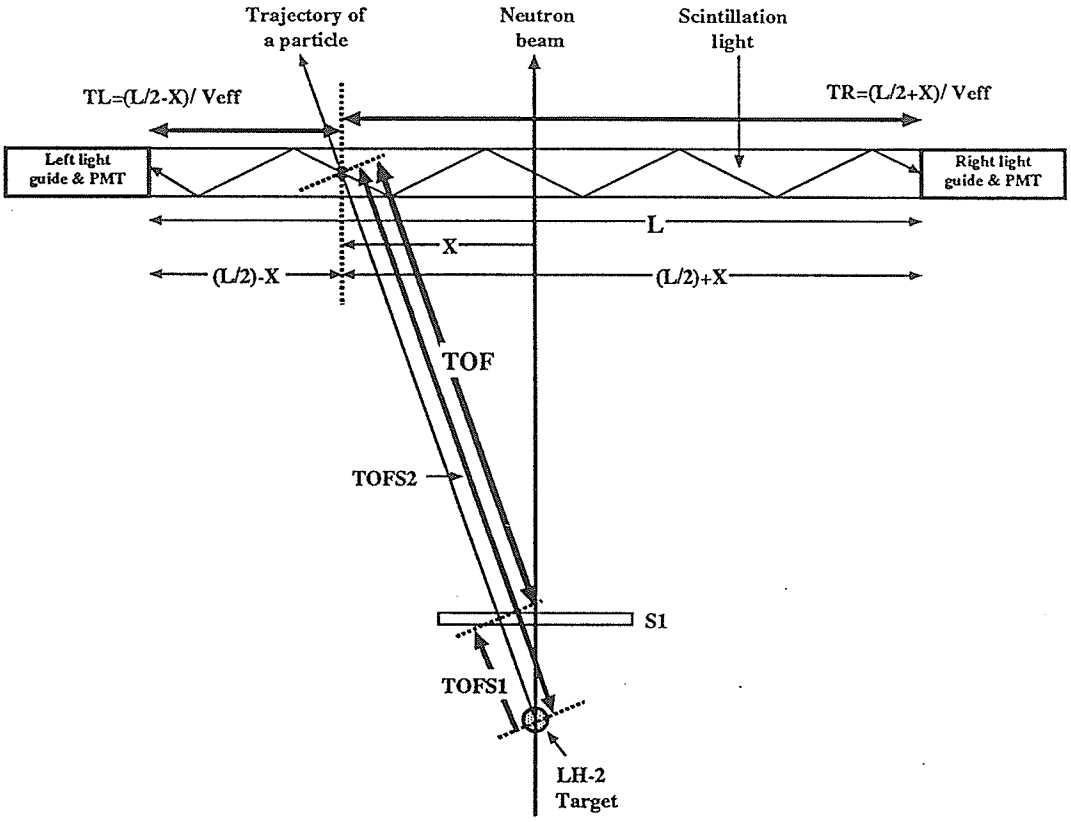


Figure 3.2: A schematic diagram of time and distance relationships used in the determination of the TOF and position of a charged particle.

ics, with respect to the master event trigger, can be expressed by

$$TDC_R = TOFS2 + \frac{(L/2 + X)}{V_{eff}} + TC_R \tag{3.2}$$

$$TDC_L = TOFS2 + \frac{(L/2 - X)}{V_{eff}} + TC_L \tag{3.3}$$

where $TOFS2$ is the time of flight of a particle from the $LH_2$ target to an S2 scintillator bar, $V_{eff}$ is the effective velocity of light in the scintillator, and $TC_R$ and $TC_L$ are time constants associated with a number of variables such as the time it takes the scintillation light to traverse the light guides, photomultipliers' transit times, PMT voltages, cable lengths, signal speed in the cable, etc..

### 3.3 Impact Position

The convention used to label axes is: $+Z$ is along the neutron beam, $+X$ is horizontal and to the left looking along the neutron beam, and $+Y$ is up. The impact position, $X$ of a particle along a scintillator was determined using the difference in the times of arrival of the two PMT signals, while the the $Y$ and $Z$ position were determined from the position of the scintillator. From equation 3.3 and 3.2, the $X$ position is given by

$$X = V_{eff}\left[\frac{(TDC_R - TDC_L)}{2} + TCENTER\right] \tag{3.4}$$

The absolute times with respect to the event in the target are not necessary because they drop out in the subtraction ($TDC_R$ - $TDC_L$). However, the $TCENTER$ constant which combines constants in equation 3.3 and 3.2 is not easy to measure or predict and must be calculated by calibrating against known event positions in a scintillator.

The value of $V_{eff}$ was determined by adjusting the range of positions to give the physical length of the scintillator (200 $cm$). A mean effective velocity of

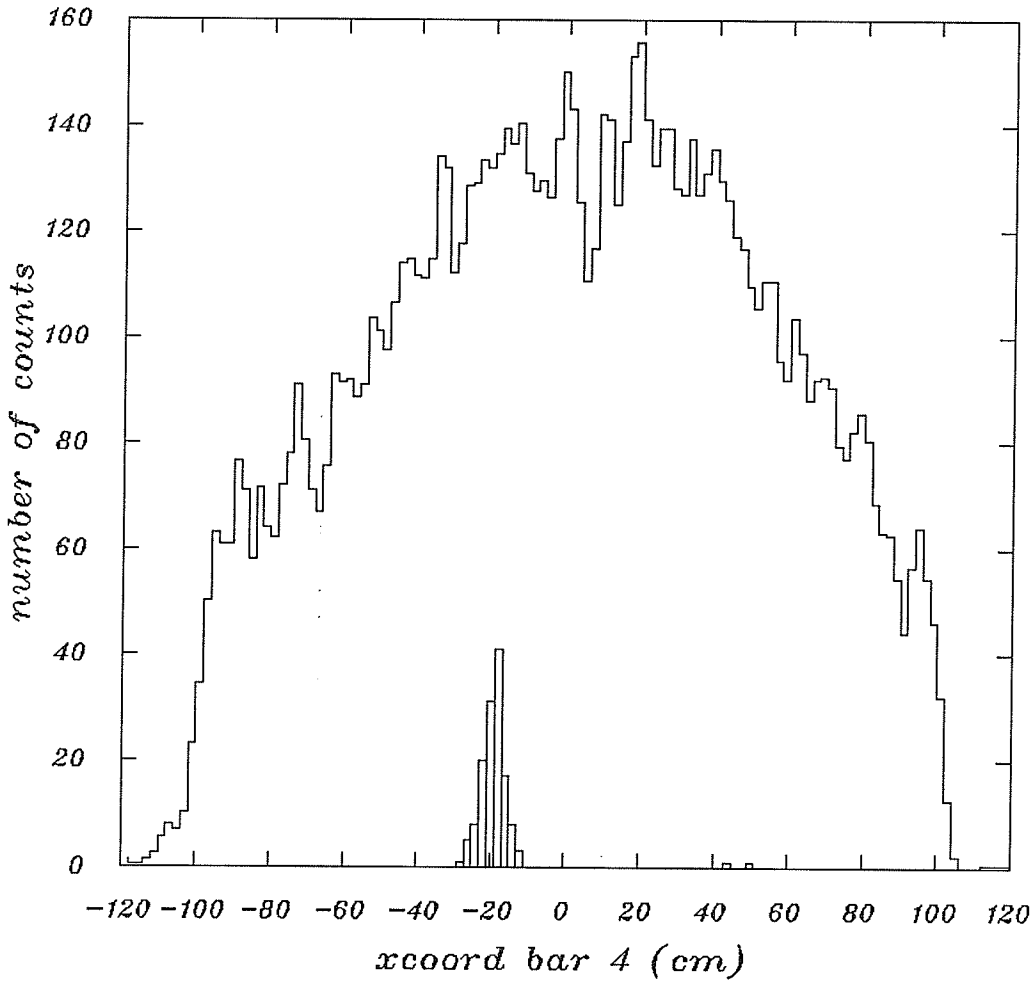


Figure 3.3: Impact positions of bar # 4 (large histogram). Events in which the button scintillator behind the bar was hit (dashed histogram).

Table 3.2: Position calibration constants

| BAR # | $TCENTER$ $[ns]$ | BAR # | $TCENTER$ $[ns]$ | BAR # | $TCENTER$ $[ns]$ |
|---|---|---|---|---|---|
| 2 | -4.20 | 8 | 1.27 | 14 | -1.32 |
| 3 | -2.26 | 9 | 4.21 | 15 | 0.44 |
| 4 | 3.00 | 10 | 1.83 | 16 | 1.62 |
| 5 | -3.26 | 11 | 2.31 | 17 | -5.01 |
| 6 | 0.80 | 12 | -2.98 | 18 | 2.07 |
| 7 | 2.56 | 13 | 1.64 | 19 | 1.20 |

$15.5 \pm 0.5$ $cm/ns$ was obtained for the S2 scintillators. The determined average value of $V_{eff}$ is smaller than the velocity of light in BC408 scintillators (which is 19 $cm/ns$ according to equation 3.1 and table 3.1) because of multiple reflections the light goes through before it reaches the PMT. However, similar values of effective velocities were obtained in other experiments using long scintillators [Bla92,Bor92].

The value of $TCENTER$ for each S2 bar was obtained by requiring events which hit the button scintillator located behind each bar to be centered at $X = -20$ $cm.$ the determined $TCENTER$ constants are given in table 3.2. Figure 3.3 shows a histogram of impact positions for one of the S2 scintillator bars, the small histogram shown (centered at $X = -20$) is for button events.

To investigate the reliability of the position calibration, the centroid of button events' position for scintillators 3 to 18 (bars 2 and 19 were not included since they do not have sufficient button events) were determined for several runs covering the period of data taking. The mean positions are almost constant for most of the bars, as can be seen from figure 3.4, except for one bar, bar number 15, which

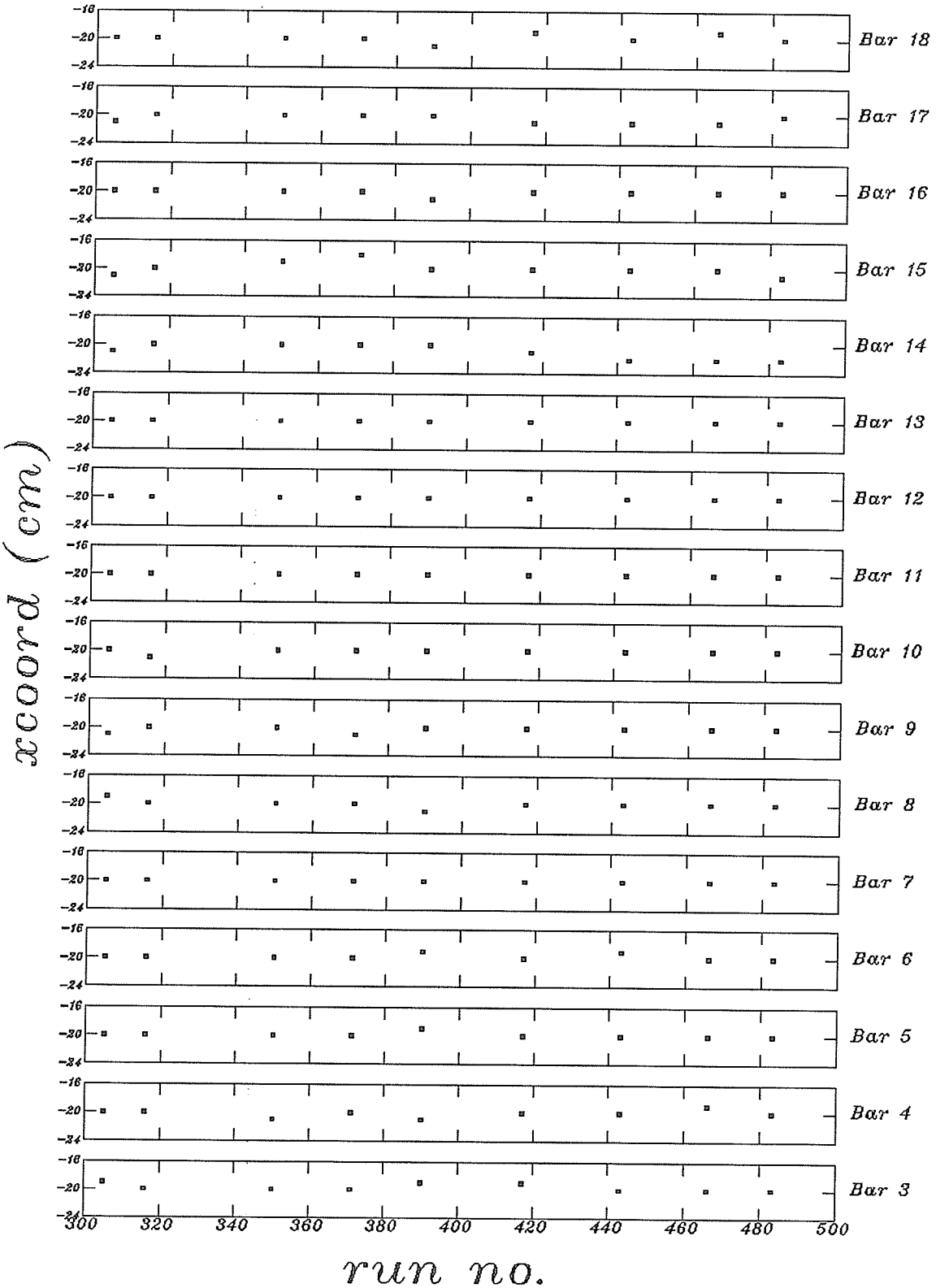


Figure 3.4: A plot of mean position of button events vs. run number.

experienced an appreciable drift in the electronics.

## 3.4 Time Of Flight

From equation 3.2 and 3.3, the time of flight of a charged particle between the $LH_2$ target and a scintillator bar is

$$TOFS2 = \frac{(TDC_R + TDC_L)}{2} + TOFFSETS2 \tag{3.5}$$

In a similar fashion, the time of flight of a particle between the $LH_2$ target and the TOF start scintillator S1 can be given by

$$TOFS1 = \frac{(TDC_U + TDC_D)}{2} + TOFFSETS1 \tag{3.6}$$

where U and D refer to the up and down photomultipliers viewing S1. Thus, the TOF of a particle between S1 and S2 is

$$TOF = \frac{(TDC_R + TDC_L)}{2} - \frac{(TDC_U + TDC_D)}{2} + TOFFSET \tag{3.7}$$

where $TOFFSET$ is a calibration constant which allows the determination of the absolute $TOF$.

$TOFFSET$ can be determined by comparing the $TOF$ obtained experimentally to that predicted theoretically for a particle with known energy scattering at the same angle. Several types of events, producing particles with known speed and hence $TOF$, are available and could be utilized in this calibration. They include:

1. Elastically scattered protons from $np \rightarrow np$. During the course of the experiment, several runs consisting mainly of elastic scattering data were taken and dedicated to calibration purposes.

2. Electrons from $\pi^0$ gamma rays. However, these events are only present in the central bars.

3. Reconstructed 3-prong events from $np \rightarrow pp\pi^-$. They are available if the $\pi^-$ was also detected in the forward direction.

In addition, events in which one particle triggers two adjacent bars, "*cross talk*", may also be used to compare the calibration of neighboring bars. It was decided that the first type of events would be used, since they cover the whole region of the S2 array, and they are more available.

The speed of the elastic protons was determined by fitting a function of the form

$$SPEED_{th} = a + b\,\theta + c\,\theta^2 \tag{3.8}$$

to the kinematics data of protons originating from $np \rightarrow np$ with neutrons of 438 $MeV$. $\theta$ is the laboratory angle of the recoil proton in degrees, and the constants $a$, $b$, and $c$ have the values $a = 21.8\ cm/ns$, $b = 2.0 \times 10^{-2}\ cm/ns$, and $c = -2.9 \times 10^{-3}\ cm/ns$.

Figure 3.5 shows a plot of the calculated speed vs. the angle as determined by the position calculation described in the previous section. The "segmentation" of the speed into apparent vertical bars arises from the finite width of the scintillator bars (10 $cm$). The vertical position (Y) of an event was taken to be the Y position of the center of the bar for those cases in which only one bar was triggered, and to be at the boundary of the two bars when in a cross talk event (two neighbouring bars were triggered). The uncertainty in position was therefore on the order of $\pm 5$ $cm$ which is not negligible at a distance of approximately 120 $cm$ from the target.

The upper band in figure 3.5 contains high speed particles of well defined kinematics that can be used in the calibration of TOF. These particles are protons originating from $np$ elastic scattering. The lower band consists of a broader band due to inelastic processes which produce one charged particle in the final state,

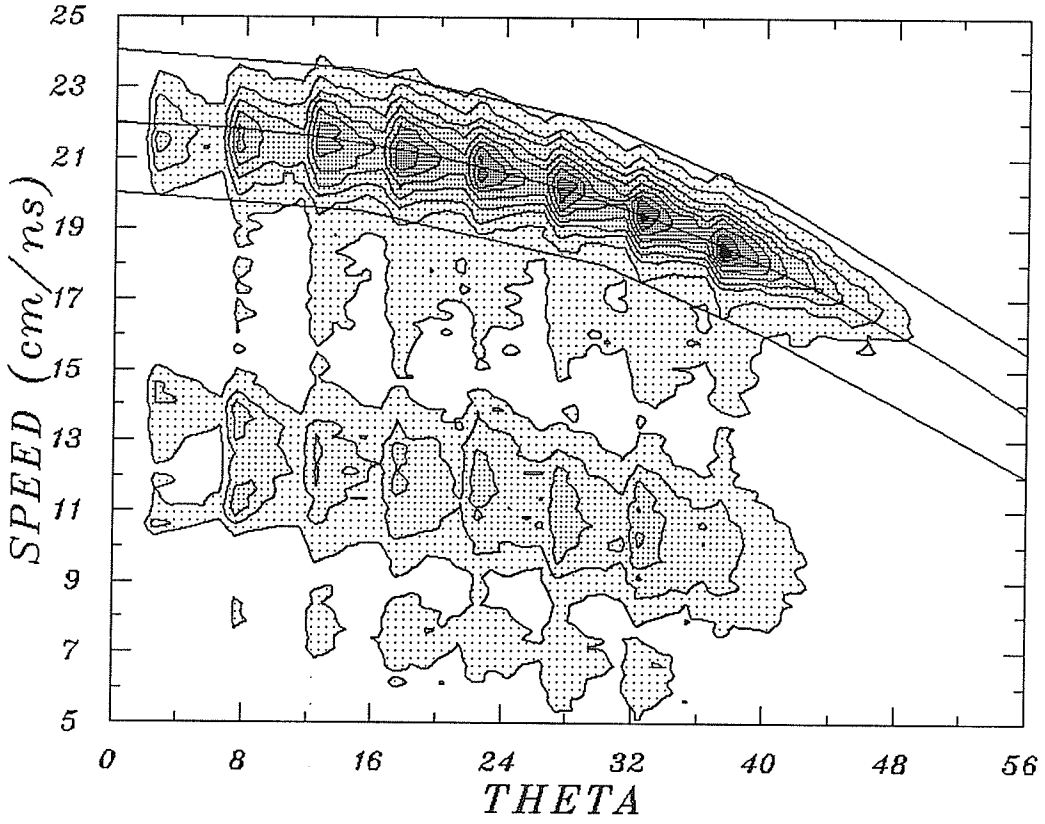


Figure 3.5: Two dimensional plot of $\theta$ vs. speed. The middle line represents the theoretical function for the speed, while the upper and lower lines represent the cuts used in selecting elastic protons.

notably $np \rightarrow np\pi^0$, and $np \rightarrow d\pi^0$.

The difference between the measured and expected $TOF$'s was calculated for events in which only one charged particle was detected. A typical distribution of this difference, for one of the S2 scintillators, is given in figure 3.6 (dotted line). The distribution shows a peak corresponding to the elastically scattered protons, followed by a tail of quasi-elastic protons, and then by a small bump corresponding to particles produced in inelastic processes.

In order to remove events corresponding to quasi-elastic and inelastic processes, a cut was applied which accepted only events in the locus representing the elastically scattered protons in the $\theta - SPEED$ scatter plot. A typical cut is shown in Figure 3.5. As a result of the cut, an almost gaussian peak (shown in figure 3.6 by the solid line) was obtained for the TOF. The $TOFFSET$ constant was determined by requiring the peak to be centered at zero. The overall time resolution of a bar was given by the standard deviation ($\sigma$), assuming that the peak is gaussian. Table 3.3 lists the overall time resolution ($\sigma$) and $TOFFSET$ constant for each bar. Bars 2, 18, and 19 had larger time resolutions due to their different dimensions.

In order to monitor the stability of the TOF calibration from run to run, the TOF difference (discussed above) was determined for each scintillator using button events alone. It was found that the TOF calibration remained very stable during the whole course of the experiment, as can be seen from figure 3.7.

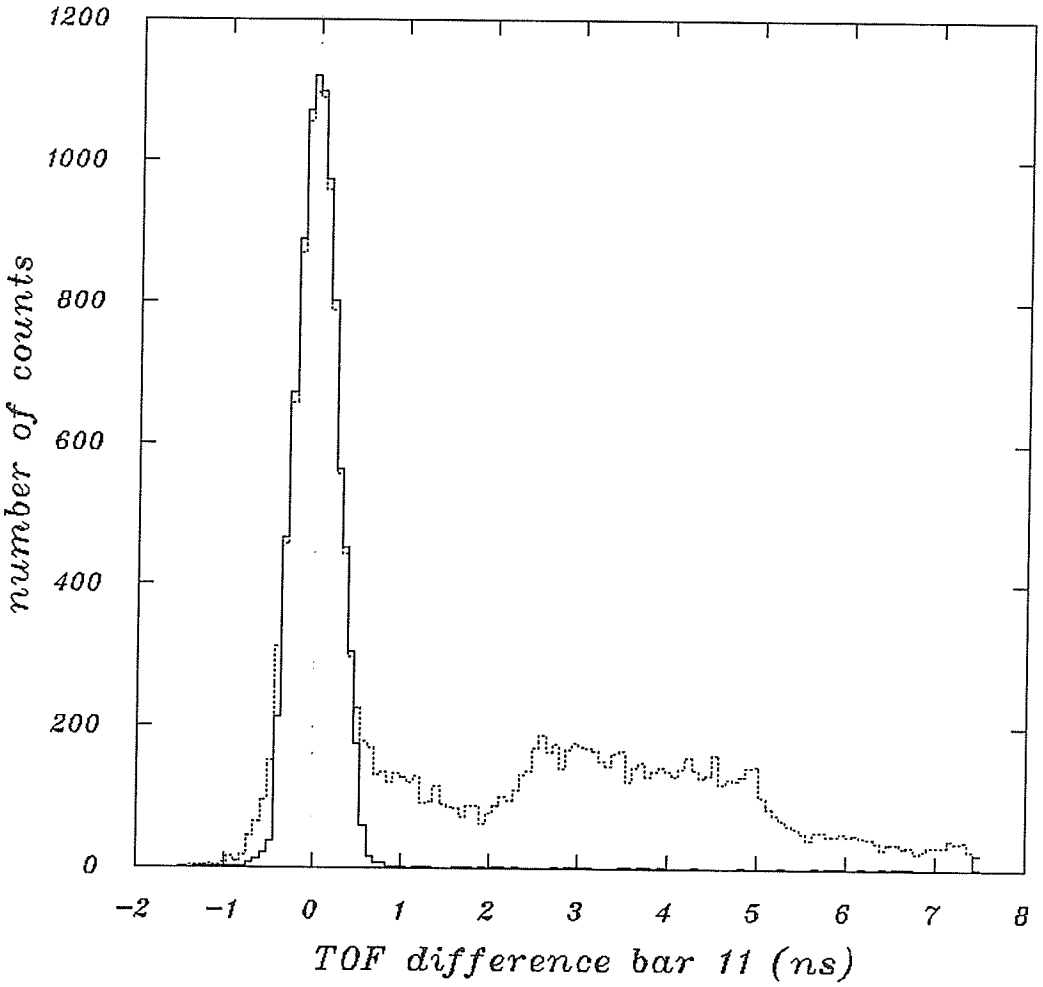


Figure 3.6: Histograms of $(TOF_{th} - TOF_{ex})$ for all events in which one scintillator is hit (dotted line), and after using a cut which accepted only elastically scattered protons (solid line).

Table 3.3: Calibration constants and resolutions of the TOF stop bars.

| Bar # | $TOFFSET$ $[ns]$ | $\sigma$ $[ps]$ | Bar # | $TOFFSET$ $[ns]$ | $\sigma$ $[ps]$ |
|---|---|---|---|---|---|
| 2 | 51.50 | 590 | 11 | 59.24 | 215 |
| 3 | 56.58 | 273 | 12 | 61.69 | 215 |
| 4 | 61.71 | 252 | 13 | 66.45 | 227 |
| 5 | 62.00 | 237 | 14 | 63.32 | 228 |
| 6 | 58.70 | 227 | 15 | 51.81 | 215 |
| 7 | 62.26 | 226 | 16 | 58.46 | 226 |
| 8 | 60.75 | 227 | 17 | 54.66 | 234 |
| 9 | 60.64 | 224 | 18 | 55.78 | 471 |
| 10 | 60.80 | 221 | 19 | 60.70 | 597 |

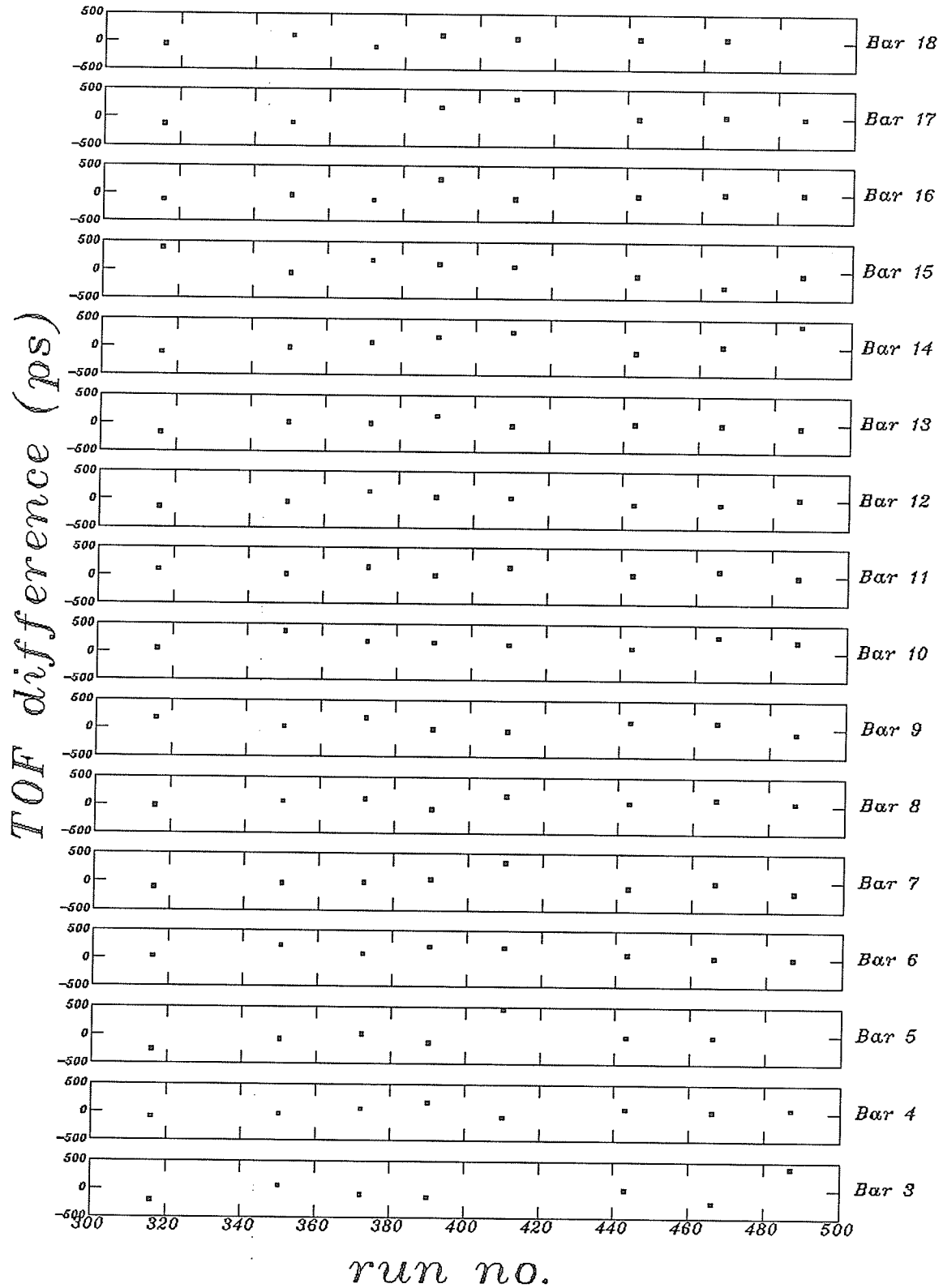


Figure 3.7: A plot of the mean TOF difference ($TOF_{th} - TOF_{ex}$) for button events vs. run number.

## 3.5 Energy Loss

The energy loss of a particle passing through the S2 scintillator bars was deduced from the integrated pulse heights of the left and right PMTs. These pulse heights (PH) were defined as the number of ADC channels above pedestals. A pulse produced at the anode of a PMT, due to the passage of a particle through a scintillator, depends mainly on the following factors:

- The energy deposited (E) in the scintillator.
- The distance from the end of the scintillator to the place where the scintillation occurred. This dependence is due the self-absorption in the scintillator, and light trapping effects mentioned in section 3.1. To correct for these effects, an exponential dependence was initially assumed as in references [Bro84,Ben90].
- The gain of both PMTs.

Thus the pulse heights of the left and right PMT can be expressed by

$$PH_L = E\ exp\left[\frac{-(L/2 - X)}{\lambda}\right] GAIN_L \tag{3.9}$$

$$PH_R = E\ exp\left[\frac{-(L/2 + X)}{\lambda}\right] GAIN_R \tag{3.10}$$

where $GAIN_L$, $GAIN_R$ are the gains of the left and right PMTs and $\lambda$ is the attenuation length.

To determine the attenuation length and the relative gains of the PMTs, the logarithm of the ratio of $PH_L$ and $PH_R$ were taken giving

$$ln\left(\frac{PH_L}{PH_R}\right) = ln\left(\frac{GAIN_L}{GAIN_R}\right) + \frac{2}{\lambda}X \tag{3.11}$$

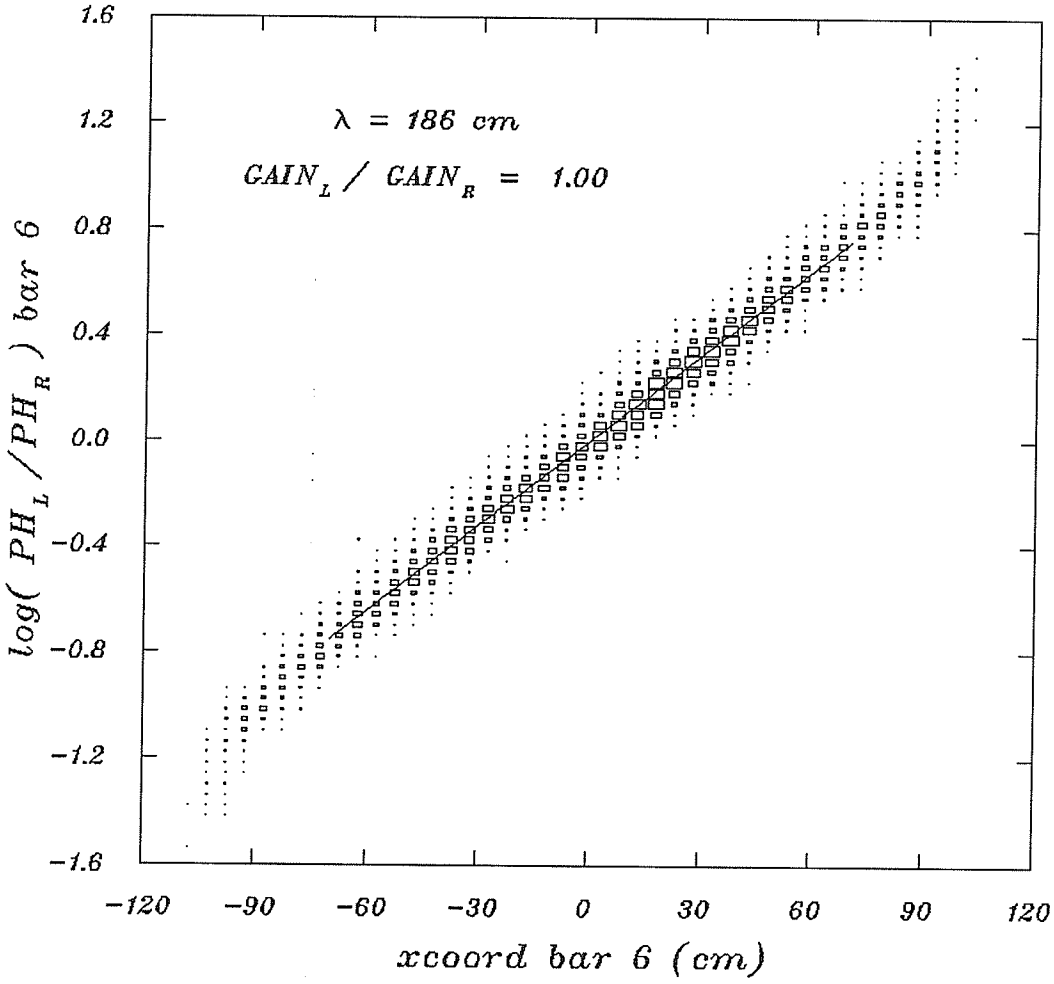


Figure 3.8: Attenuation fit for bar # 6.

A plot of $ln\left(\frac{PH_L}{PH_R}\right)$ vs. $X$ for one of the scintillator bars is shown in figure 3.8. As can be seen from this figure, the data follows a straight line except near the ends of the bar where the data starts to deviate from a straight line. The deviation occurs because the amount of light that can reach the PMT without scattering increases as the scintillation take place closer to the end of the bar. To avoid these deviation, a straight line was fitted only to the region $-70 < X < 70$. The calibration coefficients $\lambda$ and $\frac{GAIN_L}{GAIN_R}$ were extracted from the slope and intercept of the fitted line respectively. A mean attenuation length of $195 \pm 10$ $cm$ was obtained for bars 3 to 17, while a mean attenuation length of 95 $cm$ was obtained for bars 2, 18, and 19 due to their different dimensions (see table 2.3.

From equation 3.9 and 3.10, the energy deposited in a scintillator is

$$E = \sqrt{\frac{PH_L\ PH_R}{GAIN_L\ GAIN_R}\ \ exp\left(\frac{L}{\lambda}\right)} \tag{3.12}$$

The stopping power $(dE/dX)$ was calculated for every event, by dividing the energy deposited in a scintillator by the path length $(l)$ of the ionizing particle within the scintillator as it passed through. The calculated stopping power was compared to that for a recoil proton scattering elastically at the same angle. For $np$ elastically scattered protons, the theoretical $(dE/dX)_{th}$ as a function of angle $\theta$ was determined to be of the form

$$\left(\frac{dE}{dX}\right)_{th} = a + b\ \theta + c\ \theta^2 + d\ \theta^3 \tag{3.13}$$

where $a = 2.8\ MeV/cm$, $b = 2.5 \times 10^{-2}\ MeV/cm$, $c = -1.2 \times 10^{-3}\ MeV/cm$, and $d = 3.6 \times 10^{-5}\ MeV/cm$.

The cut used to select events of elastically scattered protons in section 3.4 was applied here to the ratio of $(dE/dX)_{ex}$ and $(dE/dX)_{th}$ resulting in the clean peak shown in figure 3.9. The values of $GAIN_L \times GAIN_R$ constant was determined by centering the peak of the ratio at 1. From the $GAIN_L \times GAIN_R$ values and the

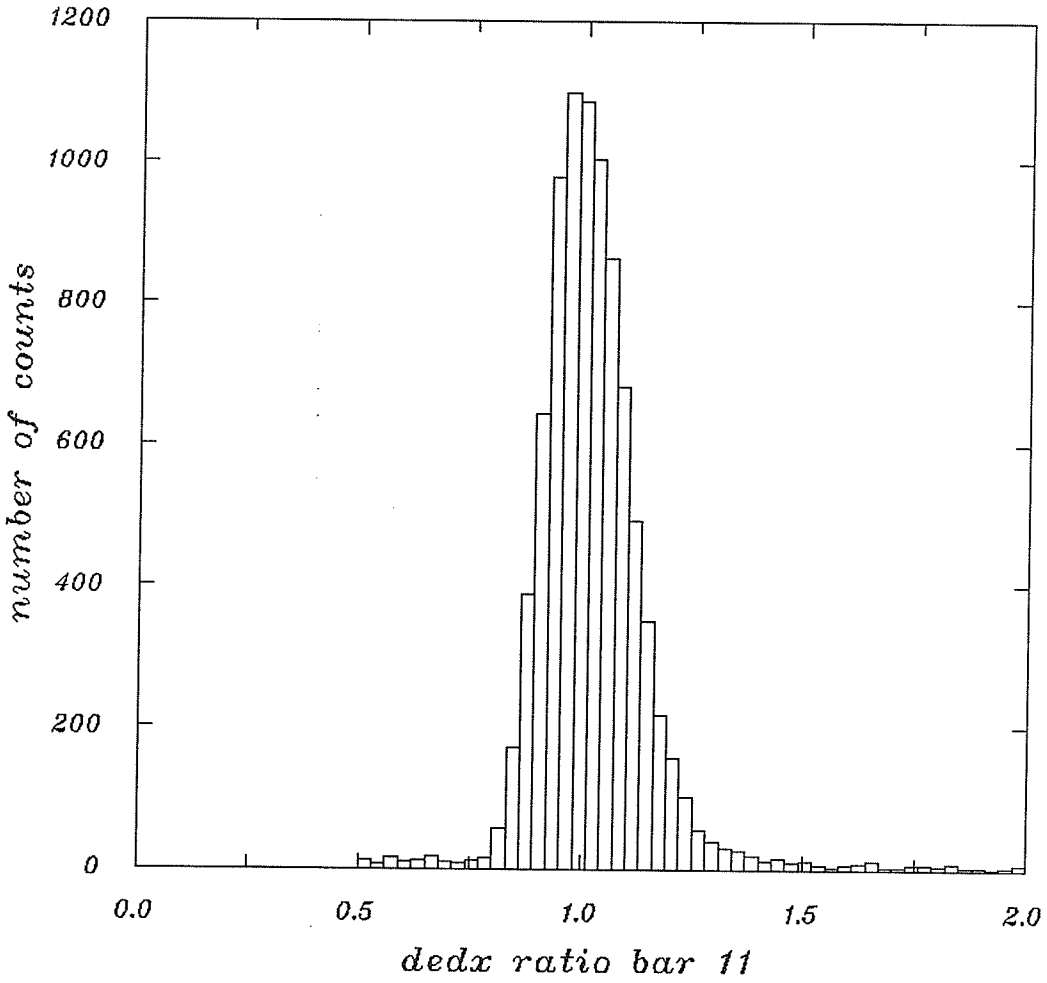


Figure 3.9: The ratio of $(dE/dX)_{th}$ and $(dE/dX)_{ex}$ for bar # 11.

values of gain ratios determined earlier, the exact gain for each PMT was obtained. Table 3.4 gives a list of all the energy calibration constants.

The ratio between the energy determined from the right PMT and that determined from the left PMT for each bar was used to investigate the stability of the gains of PMTs viewing each bars. Figure 3.10 shows such a ratio for one of the scintillator bars. If the gains were calibrated correctly and did not drift during course of the experiment, the mean energy ratio should not deviate from 1. From figure 3.11 one can see that the gains of most PMTs remained very stable (less than 2% change).

Table 3.4: Energy calibration constants

| Bar # | $PED_L$ | $PED_R$ | $GAIN_L$ | $GAIN_R$ | $\lambda$ [$cm$] |
|---|---|---|---|---|---|
| 2 | 11 | 10 | 8.6 | 7.4 | 96 |
| 3 | 11 | 11 | 4.8 | 6.0 | 218 |
| 4 | 14 | 9 | 4.6 | 4.1 | 200 |
| 5 | 9 | 9 | 5.4 | 6.3 | 201 |
| 6 | 10 | 7 | 6.1 | 6.1 | 186 |
| 7 | 9 | 8 | 5.3 | 5.6 | 184 |
| 8 | 2 | 2 | 5.1 | 6.4 | 182 |
| 9 | 7 | 8 | 6.8 | 6.5 | 205 |
| 10 | 9 | 4 | 7.7 | 7.7 | 198 |
| 11 | 8 | 7 | 6.6 | 9.6 | 223 |
| 12 | 10 | 7 | 8.9 | 11.1 | 221 |
| 13 | 10 | 9 | 6.2 | 6.0 | 212 |
| 14 | 12 | 10 | 6.6 | 5.8 | 214 |
| 15 | 10 | 9 | 6.4 | 6.5 | 213 |
| 16 | 11 | 10 | 6.8 | 7.5 | 204 |
| 17 | 11 | 10 | 7.5 | 10.0 | 216 |
| 18 | 11 | 10 | 8.8 | 5.8 | 94 |
| 19 | 10 | 8 | 4.2 | 5.2 | 96 |

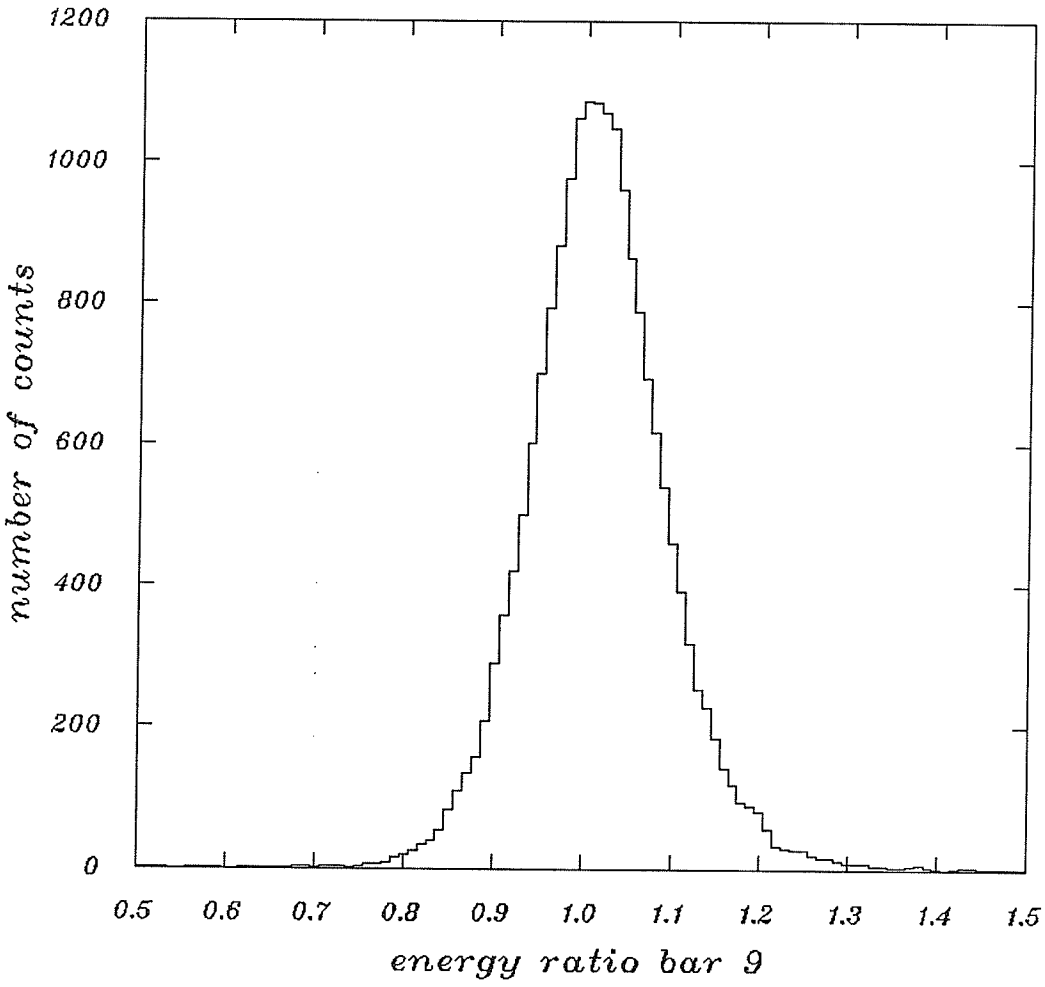


Figure 3.10: A histogram of the ratio of energies measured by the left and right photomultipliers viewing bar # 9.

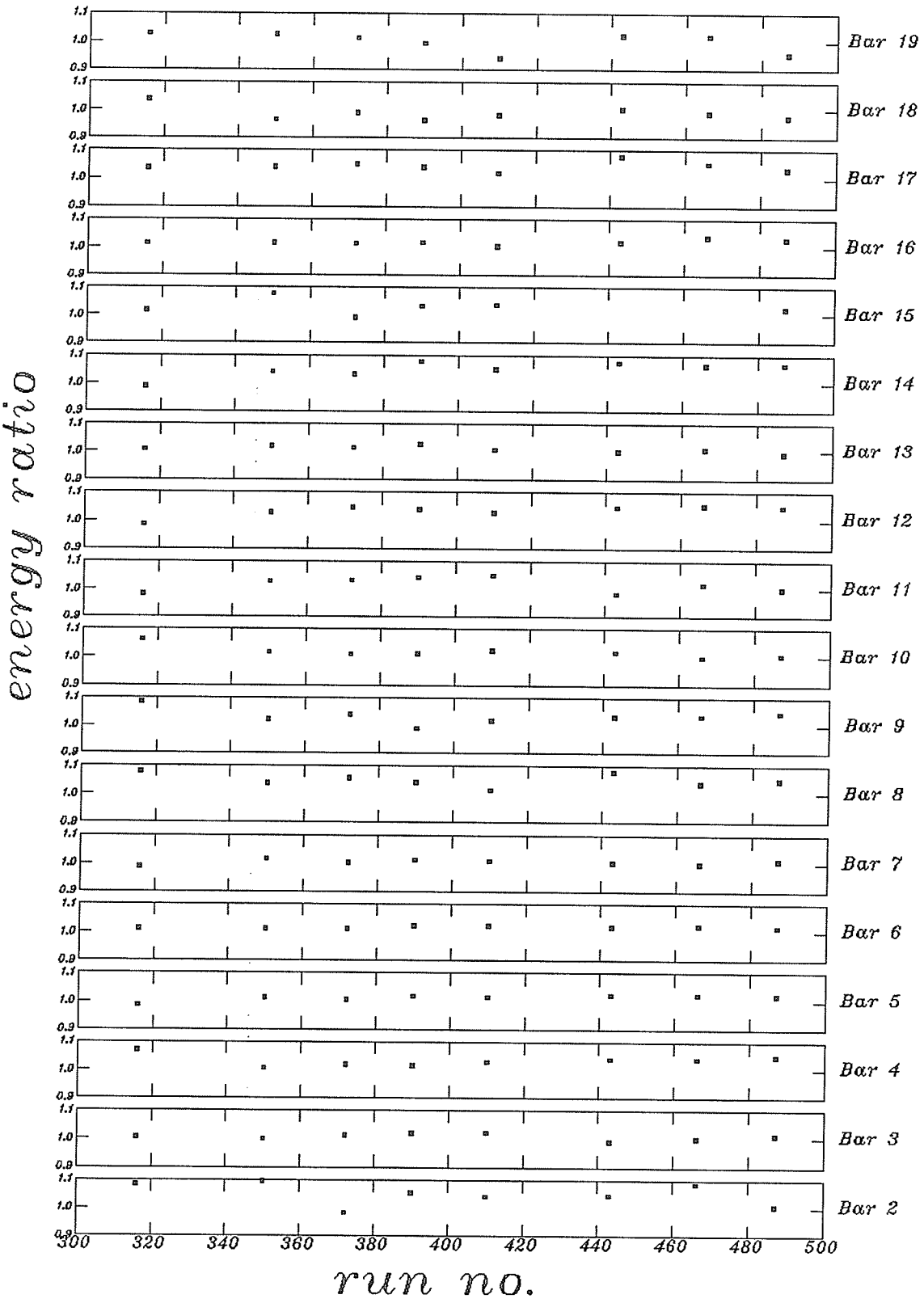


Figure 3.11: A plot of the mean energy ratio for each bar vs. run number.

# CHAPTER 4

## Conclusion

Calibration of the TOF system employed in the TRIUMF PIPROD experiment was carried out. The calibration involved the determination of constants that allow the calculation of the absolute values of:

- Impact position: two calibration constants were used; the effective velocity of light ($V_{eff}$) inside a scintillator and $TCENTER$. An average $V_{eff}$ of $15.5 \pm 0.5$ $cm/ns$ was obtained for the S2 bars, while $TCENTER$ varied from bar to bar.

- Time of flight: in the TOF calibration, only one constant, $TOFFSET$, was needed. This constant was determined for each bar using elastically scattered protons from $np \rightarrow np$. A time resolution of $\sigma = 230$ and 550 $ps$ were obtained for the 3 and 2 $cm$ thick scintillators respectively.

- Energy loss: in calibrating energy loss of a charged particle in a bar, three constants were needed; The light attenuation length ($\lambda$) and the gains of the two PMT's viewing that bar. An average attenuation length of $\lambda = 195 \pm 10$ and $95 \pm 10$ $cm$ were obtained for the 3 and 2 $cm$ thick scintillators.

The stability of the above calibration constants was monitored for the entire period of the experiment. Appendix A shows the corrected constants for several runs. It was found that the TOF system has performed well, except for one bar which experienced an appreciable electronic drifting, and a few PMTs whose gains drifted by about 5%).

# REFERENCES

# REFERENCES


[Aar68] R. Aaron, R.D. Amado, and J.E. Young, *Phys. Rev.*, 174:2022, (1968).

[Abe85] R. Abegg et al., *Nucl. Instr. & Meth.*, A234:11 , (1985).

[Abe87] R. Abegg, and R. Schubank, *In-Beam Polarimeter in BL4A and BL4B*, (TRIUMF Internal Report), TRI-DN-87-17, (1987).

[And88] V.P. Andreev et al., *Z. Phys.*, A329:371 , (1988).

[Arn88] R.A. Arndt, *SAID: an interactive dial-in program for scattering analysis.*, (1988).

[Arn90] R.A. Arndt and L.D. Roper, in *Physics With Polarized Beams On Polarized Targets*, (World Scientific) 94, (1990).

[Ben90] J.M. Benlloch, M.V. Castillo, A. Ferrer, J. Fuster, E. Higon, A. Llopis, J. Salt, E. Sanchez, E. Sanchis, E. Silvestre, and J. Cuevas, *Nucl. Instr. & Meth.*, A311:113, (1990).

[Bir64] J.B. Birks, *The Theory and Practice os Scintillation Counting*, (Pergamon Press), Oxford, (1964).

[Bla85] B. Blankleider and I.R. Afnan, *Phys. Rev.*, C31:1380 , (1985).

[Bla92] Th. Blaich et al., *Nucl. Instr. & Meth.*, A314:136 , (1992).

[Bor92] K. Borer et al., *Nucl. Instr. & Meth.*, A311:113 , (1992).

[Bro84] J.H. Brown, T.H. Burnett, V. Cook, C. Delpapa, A.L. Duncan, P.M. Mockett, J.C. Sleeman, H-J. Willutzki, and D.E. Wisiki , *Nucl. Instr. & Meth.*, 221:503, (1984).

[Buc91] L. Buchmann, *Nucl. Instr. & Meth.*, A306:413 , (1991).

[Bug87] D. Bugg and C. Wilkin, *Nucl. Phys.*, A467:575 , (1987).

[Bys87] J. Bystricky, C. Lechanoine-Leluc, and F. Lehar, *J. Phys.*, 48:199, (1987).

[Cao86] Z. Cao, and W. Hwang , *Phys. Rev.*, C34:1785 , (1986).

[Chu90] J.L. Chuma, *PLOTDATA*, (TRIUMF Internal Report), TRI-CD-87-03b, (1990).

[Dag81] G. Dagostini, G. Marini, G. Martellotti, F. Massa, A Rambaldi, and A. Sciubba *Nucl. Instr. & Meth.*, 185:49 , (1981).

[Dav90] N. Davision, in *Physics With Polarized Beams On Polarized Targets*, (World Scientific) 94, (1990).

[Dav91] N. Davision, *Proceedings of the fourth conf. on the intersections between particle and nuclear physics*, Tucson,AZ (1991).

[Dak82] L.G. Dakhno et al., *Phys. Lett.*, 114B:409 , (1982).

[Did91] J.P. Didelez et al., *Nucl. Phys.*, A535:445 , (1991).

[Dub86] J. Dubach, W.M. Kloet, R.R. Silbar, J.A. Tjon, and E. van Faassen, *Phys. Rev.*, C34:944, (1986).

[Dub87] J. Dubach, W.M. Kloet, and R.R. Silbar, *Nucl. Phys.* , A466:573, (1987).

[Fer63] E. Ferrari and F. Selleri, *Nuovo Cimento*, 27:1450, (1963).

[Fis87] H. Fischer et al., *SIN News Letter 19*, NL29 , (1987).

[Gar86] H. Garcilazo and L. Mathelitsch, *Phys. Rev.*, C34:1425 , (1986).

[Gar90] H. Garcilazo and T. Mizutani, *$\pi NN$ systems*, (World Scientific), (1990).

[Gel54] M. Gell-Mann and K.M. Watson, *Ann. Rev. Nucl. Sci.* , 4:219, (1954).

[Gre81] L.G. Greeniaus, and J. Soukup, *Polarimeter - Beam Energy Monitor*, (TRIUMF Internal Report), TRI-DN-81-1, (1981).

[Gre87] L.G. Greeniaus, *TRIUMF Kinematics Handbook - 2nd Edition*, TRIUMF, Vancouver, (1987).

[Han65] R. Handler, *Phys. Rev.*, B138:1230 , (1965).

[Har84] M. Harvey, J. Letourneux, and B. Lorazo, *Nucl. Phys.*, A424:428, (1984).

[Hos68] N. Hoshizaki, *Prog. Theor. Phys. (suppl.)*, 42:107 , (1968).

[Hur85] C.A. Hurlburt, in: *Plastic Scintillators, a Survey* , (Bicron Corp.), (1985).

[Kaz67] Y.M. Kazarinov and Y.N. Simonov, *Sov. Jour. Nucl. Phys.*, 4:100 , (1967).

[Kle80] M. Kleinschmidt et al., *Z. Phys.*, A298:253 , (1980).

[Klo80] W.M. Kloet and R.R. Silbar, *Nucl. Phys.*, A338:281 , (1980).

[Kon81] A. König and P. Kroll, *Nucl. Phys.*, A356:345 , (1981).

[Kno89] G.F. Knoll, *Radiation Detection and Measurement - 2nd edition*, John Wiley and Sons, (1989).

[Lag90] J.M. Laget, privite communication with N. Davison.

[Man58] S. Mandelstam, *Proc. Roy. Soc.*, A244:491 , (1958).

[Mat86] A. Matsuyama and T. Lee, *Phys. Rev.*, C34:1900 , (1986).

[Mat87] E.L. Mathie, *TRIUMF Users Handbook*, TRIUMF, Vancouver, (1987).

[Miz87] T. Mizutani, B Saghai, C. Fayard, and G.H. Lamot, *Phys. Rev.*, C35:667, (1987).

[Nis78] J.A. Niskanen, *Nucl. Phys.*, A298:417, (1978). and *Phys. Lett.*, 141b:301, (1984).

[Ril87] P.J. Riley et al., *Phys. Lett.*, 197B:23 , (1987).

[Ros54] A.H. Rosenfeld, *Phys. Rev.*, 96:139 , (1954).

[Set92] K. Seth, *Nucl. Phys.*, A543:421c , (1992).

[Shy88] R.L. Shypit, D.V. Bugg, D.M. Lee, M.W. McNaughton, R.R. Silbar, N.M. Stewart, A.S. Clough, C.L. Hollas, K.H. McNaughton, P. Riley, and C.A. Davis, *Phys. Rev. Lett.*, 60:901, (1988).

[Sta91] S. Stanislaus, D. Horvath, D.F. Measday, A.J. Noble, and M. Salomon, *Phys. Rev.*, C41:R1913, (1990).

[Sta91] S. Stanislaus, D. Horvath, D.F. Measday, A.J. Noble, and M. Salomon, *Phys. Rev.*, C44:2287, (1991).

[Tho81] W. Thomas et al., *Phys. Rev.*, D24:1736, (1981).

[Van84] E.E. van Faassen, and J.A. Tjon, *Phys. Rev.*, C30:285, (1984).

[Ver82] B.J. VerWest and R.A. Arndt, *Phys. Rev.*, C25:1979 , (1982).

[Yok80] A. Yokosawa, *Phys. Rep.*, 64:47 , (1980).

# APPENDICES

# APPENDIX A

## Stability of the Calibration Constants

In this appendix, the corrected calibration constants for several runs covering the entire period of data taking are given. Monitoring the stability of the calibration constants involved the use of button events; since bars 2 and 19 did not have many of these events, they were not included in the monitoring procedure.

From the errors of the calibration constants obtained in this appendix and chapter 3, the uncertainty of the following variables for most of the bars were found to be

1. Position : $\pm 4$ $cm$ near the end of a bar, and $\pm 2$ $cm$ at the center.

2. TOF : $\pm 225$ $ps$ which will result in a 10 % error in calculating the energy of 440 $MeV$ protons, and 4 % for 120 $MeV$ protons.

3. dE/dX : $\pm$ $0.2 MeV/cm$ which will result in almost the same uncertainty in calculating the energy as in the TOF method.

Table A.1: The position calibration constant, $TCENTER$ $(ns)$.

| | 316 | 350 | 372 | 443 | 466 | avg. |
|---|---|---|---|---|---|---|
| 3 | -2.25 | -2.27 | -2.28 | -2.25 | -2.26 | -2.26 ± 0.01 |
| 4 | 3.01 | 3.04 | 3.01 | 2.98 | 2.98 | 3.00 ± 0.02 |
| 5 | -3.27 | -3.24 | -3.25 | -3.27 | -3.26 | -3.26 ± 0.01 |
| 6 | 0.80 | 0.82 | 0.80 | 0.78 | 0.82 | 0.80 ± 0.02 |
| 7 | 2.55 | 2.55 | 2.58 | 2.58 | 2.58 | 2.56 ± 0.02 |
| 8 | 1.27 | 1.28 | 1.28 | 1.26 | 1.27 | 1.27 ± 0.01 |
| 9 | 4.20 | 4.22 | 4.23 | 4.21 | 4.22 | 4.21 ± 0.01 |
| 10 | 1.85 | 1.82 | 1.82 | 1.82 | 1.82 | 1.83 ± 0.01 |
| 11 | 2.32 | 2.34 | 2.31 | 2.29 | 2.30 | 2.31 ± 0.02 |
| 12 | -2.98 | -3.00 | -2.99 | -2.97 | -2.97 | -2.98 ± 0.01 |
| 13 | 1.64 | 1.65 | 1.63 | 1.62 | 1.64 | 1.64 ± 0.01 |
| 14 | -1.38 | -1.36 | -1.37 | -1.27 | -1.26 | -1.32 ± 0.06 |
| 15 | 0.03 | 0.45 | 0.47 | 0.64 | 0.63 | 0.44 ± 0.25 |
| 16 | 1.62 | 1.63 | 1.64 | 1.63 | 1.61 | 1.62 ± 0.01 |
| 17 | -5.05 | -5.02 | -5.01 | -4.99 | -4.99 | -5.01 ± 0.02 |
| 18 | 2.09 | 2.08 | 1.99 | 2.07 | 2.03 | 2.05 ± 0.04 |

Table A.2: The TOF calibration constant, $TOFFSET$ $(ns)$.

| | 316 | 350 | 372 | 443 | 466 | avg. |
|---|---|---|---|---|---|---|
| 3 | 56.81 | 56.54 | 56.68 | 56.61 | 56.36 | 56.60 ± 0.17 |
| 4 | 61.79 | 61.73 | 61.65 | 61.64 | 61.69 | 61.70 ± 0.06 |
| 5 | 62.16 | 61.97 | 61.98 | 61.93 | 61.93 | 62.00 ± 0.10 |
| 6 | 58.77 | 58.56 | 58.61 | 58.72 | 58.77 | 58.69 ± 0.10 |
| 7 | 62.30 | 62.23 | 62.27 | 62.30 | 62.22 | 62.26 ± 0.04 |
| 8 | 60.82 | 60.74 | 60.64 | 60.76 | 60.70 | 60.73 ± 0.07 |
| 9 | 60.63 | 60.56 | 60.46 | 60.68 | 60.69 | 60.60 ± 0.10 |
| 10 | 60.94 | 60.63 | 60.60 | 60.91 | 60.71 | 60.76 ± 0.16 |
| 11 | 59.19 | 59.28 | 59.08 | 59.27 | 59.20 | 59.20 ± 0.08 |
| 12 | 61.74 | 61.65 | 61.54 | 61.68 | 61.68 | 61.66 ± 0.07 |
| 13 | 66.58 | 66.39 | 66.45 | 66.40 | 66.42 | 66.45 ± 0.08 |
| 14 | 63.40 | 63.32 | 63.26 | 63.29 | 63.29 | 63.31 ± 0.05 |
| 15 | 51.42 | 51.85 | 51.63 | 51.89 | 52.08 | 51.77 ± 0.25 |
| 16 | 58.52 | 58.43 | 58.58 | 58.50 | 58.40 | 58.49 ± 0.07 |
| 17 | 54.72 | 54.69 | 54.58 | 54.63 | 54.58 | 54.64 ± 0.06 |
| 18 | 55.86 | 55.71 | 55.89 | 55.81 | 55.75 | 55.80 ± 0.07 |

Table A.3: Gains of the left PMT's on each bar.

| | 316 | 350 | 372 | 443 | 466 | avg. |
|---|---|---|---|---|---|---|
| 3 | 4.6 | 4.8 | 4.7 | 4.8 | 5.2 | $4.8 \pm 0.2$ |
| 4 | 4.3 | 4.8 | 4.7 | 4.6 | 4.5 | $4.6 \pm 0.2$ |
| 5 | 5.4 | 5.6 | 5.2 | 5.4 | 5.2 | $5.4 \pm 0.2$ |
| 6 | 6.0 | 6.2 | 6.0 | 6.0 | 6.0 | $6.0 \pm 0.1$ |
| 7 | 5.4 | 5.2 | 5.5 | 5.3 | 5.5 | $5.4 \pm 0.1$ |
| 8 | 5.0 | 5.0 | 4.8 | 5.0 | 5.0 | $5.0 \pm 0.1$ |
| 9 | 6.7 | 6.9 | 7.0 | 6.6 | 6.6 | $6.8 \pm 0.2$ |
| 10 | 7.4 | 7.9 | 8.0 | 7.1 | 7.2 | $7.5 \pm 0.4$ |
| 11 | 6.7 | 6.4 | 6.7 | 6.4 | 6.7 | $6.6 \pm 0.2$ |
| 12 | 9.0 | 8.8 | 9.0 | 8.9 | 8.8 | $8.9 \pm 0.1$ |
| 13 | 6.0 | 6.1 | 6.2 | 6.2 | 6.1 | $6.1 \pm 0.1$ |
| 14 | 6.6 | 6.6 | 6.7 | 6.5 | 6.4 | $6.6 \pm 0.1$ |
| 15 | 6.6 | 6.1 | 6.6 | 5.8 | 6.1 | $6.2 \pm 0.3$ |
| 16 | 6.6 | 6.8 | 6.8 | 7.0 | 6.9 | $6.8 \pm 0.1$ |
| 17 | 7.0 | 7.2 | 7.2 | 7.1 | 7.6 | $7.2 \pm 0.2$ |
| 18 | 8.4 | 8.8 | 8.2 | 7.8 | 9.6 | $8.5 \pm 0.7$ |

Table A.3: Gains of the right PMT's on each bar.

| | 316 | 350 | 372 | 443 | 466 | avg. |
|---|---|---|---|---|---|---|
| 3 | 5.8 | 6.0 | 6.0 | 5.9 | 6.5 | $6.0 \pm 0.3$ |
| 4 | 3.9 | 4.1 | 4.1 | 4.1 | 4.0 | $4.0 \pm 0.1$ |
| 5 | 6.2 | 6.5 | 6.1 | 6.4 | 6.1 | $6.3 \pm 0.2$ |
| 6 | 6.0 | 6.2 | 6.0 | 6.0 | 6.0 | $6.0 \pm 0.1$ |
| 7 | 5.6 | 5.6 | 5.8 | 5.6 | 5.8 | $5.7 \pm 0.1$ |
| 8 | 6.4 | 6.2 | 6.2 | 6.5 | 6.3 | $6.3 \pm 0.1$ |
| 9 | 6.7 | 6.5 | 6.7 | 6.3 | 6.2 | $6.5 \pm 0.2$ |
| 10 | 7.8 | 8.0 | 8.0 | 7.1 | 7.1 | $7.6 \pm 0.4$ |
| 11 | 9.5 | 9.4 | 9.9 | 9.1 | 9.8 | $9.5 \pm 0.3$ |
| 12 | 10.7 | 10.9 | 11.3 | 11.3 | 11.2 | $11.1 \pm 0.3$ |
| 13 | 5.8 | 5.9 | 6.0 | 6.0 | 5.9 | $5.9 \pm 0.1$ |
| 14 | 5.5 | 5.7 | 5.8 | 5.9 | 5.7 | $5.7 \pm 0.1$ |
| 15 | 6.4 | 6.4 | 6.3 | 6.4 | 6.6 | $6.4 \pm 0.1$ |
| 16 | 7.3 | 7.6 | 7.5 | 7.7 | 7.7 | $7.6 \pm 0.2$ |
| 17 | 9.2 | 9.5 | 9.7 | 9.8 | 10.2 | $9.7 \pm 0.3$ |
| 18 | 5.8 | 5.6 | 5.4 | 5.2 | 6.3 | $5.6 \pm 0.4$ |